Monthly Notices
of the
ROYAL ASTRONOMICAL SOCIETY
MNRAS **493,** 2377–2394 (2020) doi:10.1093/mnras/staa282

Precision angular diameters for 16 southern stars with VLTI/PIONIER

Adam D. Rains [1]★ Michael J. Ireland [1] Timothy R. White,[2] Luca Casagrande [1,3] and I. Karovicova[4]

[1]*Research School of Astronomy and Astrophysics, Australian National University, Canberra, ACT 2611, Australia*
[2]*Sydney Institute for Astronomy (SIfA), School of Physics, University of Sydney, NSW 2006, Australia*
[3]*ARC Centre of Excellence for All Sky Astrophysics in 3 Dimensions (ASTRO 3D), Australia*
[4]*Landessternwarte, University of Heidelberg Königstuhl 12, D-69117 Heidelberg, Germany*

Accepted 2020 January 27. Received 2020 January 20; in original form 2019 December 13

ABSTRACT

In the current era of *Gaia* and large, high signal-to-noise stellar spectroscopic surveys, there is an unmet need for a reliable library of fundamentally calibrated stellar effective temperatures based on accurate stellar diameters. Here, we present a set of precision diameters and temperatures for a sample of 6 dwarf, 5 sub-giant, and 5 giant stars observed with the PIONIER beam combiner at the VLTI. Science targets were observed in at least two sequences with five unique calibration stars each for accurate visibility calibration and to reduce the impact of bad calibrators. We use the standard PIONIER data reduction pipeline, but bootstrap over interferograms, in addition to employing a Monte Carlo approach to account for correlated errors by sampling stellar parameters, limb darkening coefficients, and fluxes, as well as predicted calibrator angular diameters. The resulting diameters were then combined with bolometric fluxes derived from broad-band *Hipparcos–Tycho* photometry and MARCS model bolometric corrections, plus parallaxes from *Gaia* to produce effective temperatures, physical radii, and luminosities for each star observed. Our stars have mean angular diameter and temperatures uncertainties of 0.8 per cent and 0.9 per cent, respectively, with our sample including diameters for 10 stars with no pre-existing interferometric measurements. The remaining stars are consistent with previous measurements, with the exception of a single star which we observe here with PIONIER at both higher resolution and greater sensitivity than was achieved in earlier work.

Key words: standards – techniques: interferometric – stars: fundamental parameters.

1 INTRODUCTION

Precision determination of fundamental stellar properties is a critical tool in the astronomers' toolkit in their mission to understand the night sky. Among the most useful of these properties are the effective temperature (or surface temperature) and physical radius of a star, which, for an individual star, provides insight into its evolutionary state, and aids in the understanding of exoplanetary systems – particularly for putting limits on stellar irradiation or for situations where planet properties are known only relative to their star, as is the case for radii from transits (e.g. Baines et al. 2008; van Belle & von Braun 2009; von Braun et al. 2011, 2012). More broadly, when looking at populations of stars, well-constrained parameters offer observational constraints for stellar interior and evolution models (e.g. Andersen 1991; Torres, Andersen & Giménez 2010; Piau et al. 2011; Chen et al. 2014), the calibration of empirical relations (e.g. the photometric colour–temperature scale, Casagrande et al. 2010), and detailed study of exoplanet population demographics (e.g. Howard et al. 2012; Fressin et al. 2013; Petigura, Howard & Marcy 2013; Fulton & Petigura 2018). However, the utility of knowing these properties precisely is matched by the difficulty inherent in measuring them. Precision observations are complicated, and most methods exist only as indirect probes of these properties, or have substantial model dependencies, limiting us to only a small subset of the stars in the sky.

Long-baseline optical interferometry, with its high spatial resolutions, is one such technique, capable of *spatially resolving* the photospheric discs of the closest and largest of stars. These arrays of telescopes have resolutions an *order of magnitude* better than the world's current largest optical telescopes fed by extreme adaptive optics systems (∼10 mas), and several orders of magnitude better than those unable to correct for the effect of atmospheric seeing at all (∼1–2 arcsec). This amounts to a resolution finer than 0.5–1.0 mas for modern interferometers, with typical errors of a few per cent. When combined with bolometric flux measurements and precision parallaxes, temperature and physical radii can be determined with a similar few per cent level of precision (e.g. Huber et al. 2012; Karovicova et al. 2018; White et al. 2018).

★ E-mail: adam.rains@anu.edu.au

Increasing the sample of stars with fundamentally calibrated effective temperatures is critical in the era of *Gaia* (Gaia Collaboration 2016) and ground-based high-SNR spectroscopic surveys such as *GALAH* (De Silva et al. 2015), *APOGEE* (Allende Prieto et al. 2008), and the upcoming *SDSS-V* (Kollmeier et al. 2017)). Internal errors on modern techniques for spectroscopic temperature determination are at the level of < 1.5 per cent (e.g. using the Cannon, Ho et al. 2016, trained on values from more fundamental techniques, see Nissen & Gustafsson 2018 for a summary), meaning that in order to be useful, diameter calibration at the level of < 1 per cent is required to put these surveys on an absolute scale. Whilst possible to measure $T_{\rm eff}$ spectroscopically, it is not yet possible to calibrate temperature scales at the < 100 K level from spectra alone (particularly when using different analysis techniques, e.g. Lebzelter et al. 2012), as non-local thermodynamic equilibrium and 3D effects become important, and particularly for where $\log g$ and [Fe/H] remain uncertain (e.g. Yong et al. 2004; Bensby, Feltzing & Oey 2014). Angular diameters offer a direct approach to determining $T_{\rm eff}$ when combined with precision flux measurements, such as those readily available from the *Hipparcos–Tycho* (Høg et al. 2000), *Gaia* (Gaia Collaboration 2016; Brown et al. 2018), and *WISE* (Wright et al. 2010) space missions.

Here, we present precision angular diameters, effective temperatures, and radii for 16 southern dwarf and subgiant stars, 10 of which have no prior angular diameter measurements. We accomplish this using PIONIER, the Precision Integrated-Optics Near-infrared Imaging ExpeRiment (Bouquin et al. 2011), the shortest-wavelength (H-band, $\lambda{\sim}1.6$ μm), highest precision beam combiner at the Very large Telescope Interferometer (VLTI), on the longest available baselines in order to extend the very small currently available library of 1 per cent level diameters.

2 OBSERVATIONS AND DATA REDUCTION

2.1 Target selection

The primary selection criteria for our target sample was for southern dwarf or subgiant stars lacking existing precision interferometric measurements with predicted angular diameters > 1.0 mas such that they could be sufficiently resolved using the longest baselines of the VLTI. Stars were checked for known multiplicity using *SIMBAD*, the *Washington Double Star Catalogue* (Mason et al. 2001), the *Sixth Catalog of Orbits of Visual Binary Stars* (Hartkopf, Mason & Worley 2001), and the *9th Catalogue of Spectroscopic Binary Orbits* (Pourbaix et al. 2004) and ruled out accordingly. The list of science targets can be found in Table 1 along with literature spectroscopic $T_{\rm eff}$, $\log g$, and [Fe/H]. All targets are brighter than $H \sim 3.1$, limiting available high-precision photometry to the space-based *Hipparcos-Tycho*, *Gaia*, and *WISE* missions, with *2MASS* notably being saturated for most targets. Where uncertainties on $\log g$, and [Fe/H] were not available, conservative uncertainties of 0.2 dex and 0.1 dex were adopted, respectively.

Fig. 1 presents a $(B - V)$ colour–magnitude diagram of the same targets using *Tycho-2* $B_{\rm T}$ and $V_{\rm T}$ photometry (converted using the relations from Bessell 2000), and *Gaia* DR2 parallaxes to calculate the absolute $V_{\rm T}$ magnitudes. Overplotted are ∼Solar metallicity ($Z = 0.058$) BASTI evolutionary tracks (Pietrinferni et al. 2004). Given that these targets are within the extent of the Local Bubble ($\lesssim 70$ pc, e.g. Leroy 1993; Lallement et al. 2003), we assume that they are unreddened. Distances are calculated incorporating the systematic parallax offset of -82 ± 33 μas found by Stassun & Torres (2018).

τ Cet, ϵ Eri, δ Eri, 37 Lib, and β Aql form part of an overlap sample with the PAVO beam combiner (Ireland et al. 2008) on the northern CHARA array (ten Brummelaar et al. 2005), with diameters to be published in White et al. (in preparation) enabling consistency checks between the northern and southern diameter sample.

2.2 Calibration strategy

The principal data product for the interferometric measurement of stellar angular diameter measurements is the *fringe visibility*, V, which can be defined as the ratio of the *amplitude* of interference fringes, and their *average intensity* as follows:

$$V = \frac{\text{fringe amplitude}}{\text{average fringe intensity}}, \tag{1}$$

where V varies between 0, for completely resolved targets (e.g. resolved discs, well-separated binary components), and 1 for completely unresolved targets (i.e. a point source). V is a function of both the projected baseline and the wavelength of observation, combining to give a characteristic *spatial frequency* at which observations are made.

When performing ground-based interferometric observations in real conditions, the combined effect of atmospheric turbulence and instrumental factors (e.g. optical aberrations) is to reduce the measured science target visibility $V_{\rm sci,\,measured}$ from its true value. To account for this, calibrator stars are observed to obtain a measure of the combined atmospheric and instrumental transfer function $V_{\rm system}$ in order to calibrate the $V_{\rm sci,\,measured}$ and determine their true value of $V_{\rm sci,\,corrected}$. Ideal calibrators meet four criteria: they are single unresolved point sources to the interferometer, have no close companions or other asymmetries (e.g. oblate due to rapid rotation), and are both proximate on sky and close in magnitude to the science target. Being close on sky ensures they are similarly affected by atmospheric turbulence (and thus suffer from the same systematics), and similar in magnitude ensures the detector can be operated in the same mode (e.g. same exposure time and gain). Their status of isolated or single stars means that their observation is insensitive to projected baseline geometry.

With all of these criteria met, and calibrator observations taking place immediately before or after science target observations, the measured calibrator visibility $V_{\rm cal,\,measured}$ can be used to determine $V_{\rm system}$ provided a prediction of the *true* calibrator visibility $V_{\rm cal,\,predicted}$ is available in the form of a predicted limb darkened angular diameter $\theta_{\rm LD,\,cal}$. In practice the significance of the dependency on knowing the (typically unmeasured) diameter of a calibrator is minimized by choosing calibrators much smaller in angular size than their respective science targets (ideally $\theta_{\rm LD,cal} \leq \frac{1}{2}\theta_{\rm LD,sci}$ in practice), such that even large $\theta_{\rm LD,\,cal}$ uncertainties do not significantly change $V_{\rm cal,\,measured}$ for the mostly/entirely unresolved calibrator. This is formalized below in equations (2) and (3):

$$V_{\rm sci,corrected} = \frac{V_{\rm tar,measured}}{V_{\rm system}} \tag{2}$$

with

$$V_{\rm system} = \frac{V_{\rm cal,measured}}{V_{\rm cal,predicted}}. \tag{3}$$

This is not feasible in practice, particularly for stars as bright as those considered here, where it is difficult to find unresolved (yet bright) neighbouring stars. Given this limitation, the decision was made to observe a total of five calibrators per science target

Table 1. Science targets.

Star	HD	RA[a] (hh mm ss.ss)	Dec.[a] (dd mm ss.ss)	SpT[b]	V_T^c (mag)	H^d (mag)	$T_{\rm eff}$ (K)	$\log g$ (dex)	[Fe/H] (dex)	$v \sin i$ (km s^{-1})	Plx[a] (mas)	Refs
τ Cet	10700	01 44 02.23	− 16 03 58.32	G8V	3.57	1.8	5310 ± 17	4.44 ± 0.03	− 0.52 ± 0.01	1.60	277.52 ± 0.52	1,1,1,2
α Hyi	12311	01 58 46.77	− 62 25 48.93	F0IV	2.87	1.9	7165 ± 64	3.67 ± 0.20	0.07 ± 0.10	118.00	51.55 ± 0.83	3,4,4,5
χ Eri	11937	01 55 58.59	− 52 23 32.60	G8IV	3.80	1.9	5135 ± 80	3.42 ± 0.10	− 0.18 ± 0.07	4.50	57.38 ± 0.33	6,6,6,7
95 Cet A	20559	03 18 22.68	− 1 04 10.02	–	5.60	–	4684 ± 71	2.64 ± 0.14	− 0.15 ± 0.05	1.60	15.63 ± 0.18	8,8,8,9
ϵ Eri	22049	03 32 54.82	− 10 32 30.58	K2V	3.81	1.9	5049 ± 48	4.45 ± 0.09	− 0.15 ± 0.03	4.08	312.22 ± 0.47	1,1,1,10
δ Eri	23249	03 43 14.80	− 10 14 23.33	K0 + IV	3.62	1.7	5027 ± 48	3.66 ± 0.10	0.07 ± 0.03	6.79	110.22 ± 0.42	1,1,1,10
40 Eri A	26965	04 15 13.98	− 8 19 56.63	K0V	4.51	2.6	5098 ± 32	4.35 ± 0.10	− 0.36 ± 0.02	2.10	198.57 ± 0.51	1,1,1,2
37 Lib	138716	15 34 11.03	− 11 56 04.05	K1III-IV	4.72	2.3	4816 ± 70	3.05 ± 0.19	− 0.05 ± 0.06	4.50	35.19 ± 0.25	8,8,8,9
β TrA	141891	15 55 08.13	− 64 34 03.16	F1V	2.85	2.2	7112 ± 64	4.22 ± 0.07	− 0.29 ± 0.10	69.63	79.43 ± 0.58	3,11,4,10
λ Sgr	169916	18 27 58.19	− 26 34 39.01	K1IIIb	2.92	0.4	4778 ± 37	2.66 ± 0.10	− 0.11 ± 0.03	3.81	38.78 ± 0.63	12,13,12,14
δ Pav	190248	20 08 46.71	− 67 48 47.04	G8IV	3.62	2.0	5604 ± 38	4.26 ± 0.06	0.33 ± 0.03	0.32	164.05 ± 0.36	1,1,1,10
ϵ Ind	209100	22 03 29.14	− 57 12 11.15	K5V	4.83	2.3	4649 ± 74	4.63 ± 0.01	− 0.13 ± 0.06	2.00	274.80 ± 0.25	1,8,1,15
HD131977	131977	14 57 29.15	− 22 34 37.56	K4V	5.88	3.1	4507 ± 58	4.76 ± 0.06	0.12 ± 0.03	7.68	170.01 ± 0.09	16,17,17,10
η Sco	155203	17 12 09.22	− 44 45 34.45	F5IV	3.36	2.3	6724 ± 106	3.65 ± 0.20	− 0.29 ± 0.10	150.00	45.96 ± 0.44	18,4,4,19
β Aql	188512	19 55 18.84	06 24 16.90	G8IV	3.81	1.9	5062 ± 57	3.54 ± 0.14	− 0.19 ± 0.05	22.28	74.76 ± 0.36	8,8,8,10
HR7221	177389	19 09 53.30	− 69 34 31.31	K0IV	5.41	3.1	5061 ± 26	3.49 ± 0.09	− 0.05 ± 0.02	–	27.04 ± 0.09	12,12,12,–

Notes. [a]Gaia Brown et al. (2018) – note that Gaia parallaxes listed here have not been corrected for the zero-point offset.
[b]SIMBAD.
[c]Tycho Høg et al. (2000).
[d]2MASS Skrutskie et al. (2006).
References for spectroscopic $T_{\rm eff}$, $\log g$, [Fe/H], and $v \sin i$: 1. Delgado Mena et al. (2017), 2. Jenkins et al. (2011), 3. Blackwell & Lynas-Gray (1998), 4. Erspamer & North (2003), 5. Royer, Zorec & Gómez (2007), 6. Fuhrmann et al. (2017), 7. Schröder, Reiners & Schmitt (2009), 8. Ramírez, Allende Prieto & Lambert (2013), 9. Massarotti et al. (2008), 10. Martínez-Arnáiz et al. (2010), 11. Allende Prieto et al. (2004), 12. Alves et al. (2015), 13. Liu et al. (2007), 14. Hekker & Meléndez (2007), 15. Torres et al. (2006), 16. Boyajian et al. (2012b), 17. Valenti & Fischer (2005), 18. Casagrande et al. (2011), and 19. Mallik, Parthasarathy & Pati (2003).

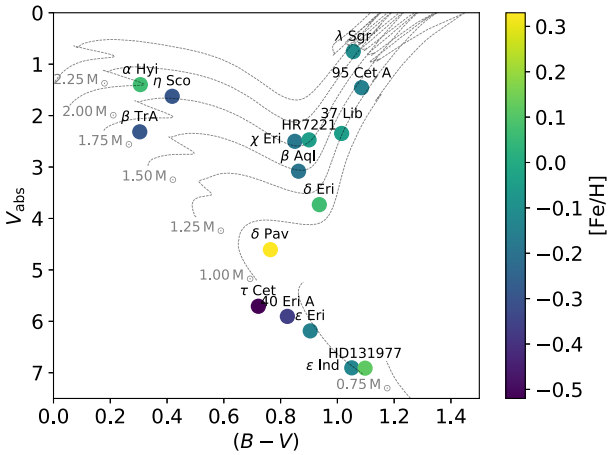

Figure 1. $(B - V)$ colour–magnitude diagram for science targets with overplotted BASTI evolutionary tracks for $Z = 0.058$.

which, on average, meet the criteria. This lead to the observation of two separate CAL-SCI-CAL-SCI-CAL sequences – one for *bright*, but often more distant and resolved, stars, and another for those more *faint*, but closer and less resolved. Calibrators from bright and faint sequences have $\theta_{\rm LD,\,cal}$, on average, $0.59\theta_{\rm LD,\,sci}$, and $0.47\theta_{\rm LD,\,sci}$, respectively. This large number of calibrators allows for the possibility of unforeseen bad calibrators (e.g. resolved binaries) without compromising on the ability to calibrate the scientific observations.

Calibrators were selected using *SearchCal*[1] (Bonneau et al. 2006, 2011), and the `pavo_ptsrc` IDL calibrator code (maintained within the CHARA/PAVO collaboration), with the list of calibrators used detailed in Table A1.

Interstellar extinction was computed for stars more distant than 70 pc using intrinsic stellar colours from Pecaut & Mamajek (2013) for the main sequence and Aller et al. (1982) for spectral types III, II, Ia, Ib, with the subgiant branch interpolated as being halfway between spectral types V and III. We note that this approach is, at best, an approximation, but more complete or modern catalogues of intrinsic stellar colours are not available, and three-dimensional dust maps (e.g. Green et al. 2015, 2018) are incomplete for the Southern hemisphere. With intrinsic colours in hand, B, V, $H_{\rm P}$, $B_{\rm T}$, $V_{\rm T}$, and $R_{\rm P}$ photometry could be corrected for the effect of reddening using the extinction law of Cardelli, Clayton & Mathis (1989) implemented in the `extinction`[2] PYTHON package. This approach was not applied to *WISE* photometry however for the joint reasons of being less subject to extinction in the infrared, and what extinction (or even emission, e.g. Fritz et al. 2011) occurs being difficult to parametrize and not covered by the same relations that hold at optical wavelengths.

Angular diameters for calibrators were predicted using surface brightness relations from Boyajian, van Belle & von Braun (2014), prioritizing those with *WISE* $W3$ or $W4$ magnitudes to minimize the effect of interstellar reddening. A $(V - W3)$ relation was used for 59 stars, the majority of our calibrator sample, with Johnson V-band magnitudes converted from *Tycho* − 2 catalogue $V_{\rm T}$ band (Høg et al. 2000) per the conversion outlined in Bessell (2000), and another three with unavailable or saturated $W3$ using a $(V - W4)$ relation.

The remaining three stars lacked *WISE* magnitudes altogether, and whilst a $(B - V)$–[Fe/H] relation (converting $B_{\rm T}$ to B, also per Bessell 2000) from Boyajian et al. (2014) was used for HD 16970A ([Fe/H] = 0.0, Gray et al. 2003), HD 20010A and HD 24555 lack literature measurements of [Fe/H] which the simpler $(B - V)$ relation is highly sensitive to. To get around both this sensitivity and the saturated nature of *2MASS* photometry for such bright stars, $(V - K)$ was computed from $(V_{\rm T} - R_{\rm P})$ via a third-order polynomial fit to the photometry of a million synthetic stars ($4,500 < T_{\rm eff} < 7,500$, $2 < \log g < 5$, $-1 < [Fe/H] < 0.5$) using the methodology and software of Casagrande & VandenBerg (2014) and Casagrande & VandenBerg (2018b). This fit was:

$$Y = 0.2892625 + 0.643771X + 2.5184359X^2 - 1.121815X^3 \quad (4)$$

where Y and X are the $(V - K)$ and $(V_{\rm T} - R_{\rm P})$ colours, respectively.

2.3 Interferometric observations

VLTI (Haguenauer et al. 2010) PIONIER (Bouquin et al. 2011) observations were undertaken in service mode during ESO periods 99, 101, and 102 (2017–2019), using the four 1.8 m Auxiliary Telescopes on the two largest configurations: A0-G1-J2-J3 and A0-G1-J2-K0 (58–132 m and 49–129 m baselines, respectively). The service mode observations had the constraint of clear skies and better than 1.2 arcsec seeing. Two 45 min CAL-SCI-CAL-SCI-CAL sequences were observed per target, with each target having five calibrator stars in total (with one shared between each sequence). In practice this looked something like CAL1-SCI-CAL2-SCI-CAL3 and CAL1-SCI-CAL4-SCI-CAL5, but with the calibrators in each sequence ordered by their respective sidereal time constraints (i.e. by taking into account shadowing from the four Unit Telescopes). PIONIER was operated in GRISM mode (6 spectral channels) for the entirety of the program.

PIONIER observations are summarized in Table 2. Note that δ Eri, 40 Eri A, and β TrA were reobserved to complete both bright and faint sequences, with both τ Cet, and ϵ Ind serving as useful interperiod diagnostics of identical sequences.

We note that all targets had sequences observed over at least two nights, with the exception of 37 Lib and β Aql which had their bright and faint sequences observed on the same night. As discussed in detail by Lachaume et al. (2019), there are correlated uncertainties for observations taken within a given night (e.g. atmospheric effects, instrumental drifts), reducing the accuracy of the resulting diameter fits. The consequence of this for these two stars is that any systematics in wavelength scale calibration are the same for both sequences.

2.4 Wavelength calibration

The accuracy of model fits to visibility measurements depends not only on the uncertainties in the observed visibilities, but also the spatial frequencies at which we measure them. The spatial frequencies here are also the working resolution of the interferometer, and any uncertainties in the baseline length or wavelength scale will affect the results. Uncertainties in the wavelength scale dominate this, with the effective wavelength conservatively having an accuracy of ±1 per cent (Bouquin et al. 2011) or even ±2 per cent (per the PIONIER manual[3]), whereas the VLTI baseline lengths are known

[1] http://www.jmmc.fr/searchcal_page.htm
[2] https://github.com/kbarbary/extinction
[3] https://www.eso.org/sci/facilities/paranal/instruments/pionier/manuals.html

Table 2. Observing log. Note that five unique calibrators were observed per science target, though some later needed to be excluded due to factors such as binarity.

Star	UT date	ESO period	Sequence type	Baseline	Calibrator HD	Calibrators used
ϵ Ind	2017-07-22	99	Faint	A0-G1-J2-K0	205935, 209952, 212878	3
α Hyi	2017-07-24	99	Faint	A0-G1-J2-K0	1581, 15233, 19319	2
χ Eri	2017-07-24	99	Bright	A0-G1-J2-K0	1581, 11332, 18622	2
β TrA	2017-07-25	99	Bright	A0-G1-J2-K0	128898, 136225, 165040	3
37 Lib	2017-07-25	99	Bright	A0-G1-J2-K0	132052, 141795, 149757	3
37 Lib	2017-07-25	99	Faint	A0-G1-J2-K0	136498, 139155, 149757	3
α Hyi	2017-07-26	99	Bright	A0-G1-J2-J3	1581, 11332, 18622	2
χ Eri	2017-07-27	99	Faint	A0-G1-J2-J3	10019, 11332, 18622	2
ϵ Ind	2017-08-17	99	Bright	A0-G1-J2-K0	197051, 209952, 219571	3
τ Cet	2017-08-17	99	Faint	A0-G1-J2-K0	9228, 10148, 18978	3
λ Sgr	2017-08-26	99	Faint	A0-G1-J2-J3	166464, 167720, 175191	2
τ Cet	2017-08-26	99	Bright	A0-G1-J2-J3	9228, 17206, 18622	2
95 Cet A	2017-08-26	99	Bright	A0-G1-J2-J3	16970A, 19994, 22484	3
δ Pav	2017-08-27	99	Faint	A0-G1-J2-J3	192531, 197051, 197359	3
95 Cet A	2017-09-01	99	Faint	A0-G1-J2-J3	16970A, 19866, 20699	3
ϵ Eri	2017-09-04	99	faint	A0-G1-J2-J3	16970A, 21530, 25725	2
40 Eri A	2017-09-04	99	Faint	A0-G1-J2-J3	24780, 26409, 27487	3
ϵ Eri	2017-09-05	99	Bright	A0-G1-J2-J3	16970A, 20010A, 24555	3
λ Sgr	2017-09-08	99	Bright	A0-G1-J2-J3	165634, 169022, 175191	2
δ Pav	2017-09-12	99	Bright	A0-G1-J2-J3	169326, 197051, 191937	3
δ Eri	2017-09-24	99	Faint	A0-G1-J2-J3	16970A, 23304, 26464	3
β TrA	2018-04-18	101	Faint	A0-G1-J2-J3	128898, 140018, 143853	3
β Aql	2018-06-04	101	Bright	A0-G1-J2-J3	182835, 189188, 194013	3
β Aql	2018-06-04	101	Faint	A0-G1-J2-J3	182835, 193329, 189533	3
ϵ Ind	2018-06-04	101	Bright	A0-G1-J2-J3	197051, 209952, 219571	3
HD131977	2018-06-05	101	Faint	A0-G1-J2-J3	129008, 133649, 133670	3
HR7221	2018-06-05	101	Bright	A0-G1-J2-J3	161955, 165040, 188228	3
ϵ Ind	2018-06-06	101	Faint	A0-G1-J2-J3	205935, 209952, 212878	3
η Sco	2018-06-06	101	Bright	A0-G1-J2-J3	135382, 158408, 160032	2
HD131977	2018-06-06	101	Bright	A0-G1-J2-J3	129502, 133627, 133670	3
HR7221	2018-06-06	101	Faint	A0-G1-J2-J3	165040, 172555, 173948	2
η Sco	2018-06-07	101	Faint	A0-G1-J2-J3	152236, 152293, 158408	1
τ Cet	2018-08-06	101	Bright	A0-G1-J2-J3	4188, 9228, 17206	3
β TrA	2018-08-07	101	Bright	A0-G1-J2-J3	128898, 136225, 165040	3
τ Cet	2018-08-07	101	Faint	A0-G1-J2-J3	9228, 10148, 18978	3
δ Eri	2018-11-25	102	Bright	A0-G1-J2-J3	16970A, 20010A, 24555	3
δ Eri	2018-11-26	102	Faint	A0-G1-J2-J3	16970A, 23304, 26464	3
40 Eri A	2018-11-26	102	Bright	A0-G1-J2-J3	26409, 26464, 33111	3
40 Eri A	2018-11-26	102	Faint	A0-G1-J2-J3	24780, 26409, 27487	3

to cm precision resulting in an uncertainty of ± 0.02 per cent for the shortest baselines.

PIONIER's spectral dispersion is known to change with time, and is calibrated once per day by the instrument operations team at Paranal. This calibration is identical to a single target observation in all respects save its use of an internal laboratory light source, with the resulting fringes used as a Fourier transform spectrometer to measure the effective wavelength of each channel. Effective wavelengths, accurate to ~ 1.5 per cent, are then assumed 'constant' for all subsequent observations that night. Calibration data were downloaded from the ESO Archive where, at least for service mode observations, they are stored under the program ID 60.A-9209(A).

Another aspect of instrumental stability to be considered is whether the piezo hardware used to construct each interferometric scan of path delay is constant with respect to time. This is not a standard part of the instrument's daily calibration routine however, and PIONIER lacks the internal laser source required to simply perform this procedure. As such, particularly given the potential for this being a limiting factor in high-precision observations, several studies have sought to investigate the stability of PIONIER via a variety of means.

Kervella et al. (2017), seeking to measure the radii and limb darkening of α Centauri A and B, were limited by this uncertainty, and spent time investigating both its magnitude and long-term stability. They used the binary system HD 123999, well constrained from two decades of monitoring (Boden, Creech-Eakman & Queloz 2000; Boden, Torres & Hummel 2005; Tomkin & Fekel 2006; Konacki et al. 2010; Behr et al. 2011), as a dimensional calibrator, and compared literature orbital solutions to those derived from their PIONIER observations. The result was a wavelength scaling factor determined through comparison of best-fitting semimajor axis values from Boden et al. (2005), Konacki et al. (2010), and the authors' of $\gamma = 1.00481 \pm 0.00412$, where γ is a multiplicative offset in the PIONIER wavelength scale, and its uncertainty the fractional standard deviation of each measurement of the semimajor axis. This uncertainty of 0.41 per cent was then added in quadrature with all derived angular diameters instead of the 2 per cent quoted in the PIONIER manual. These results were also found to be consistent

(within 0.8σ) with another binary, HD 78418, also studied by Konacki et al. (2010) yielding $\gamma = 1.00169$, though with only two points this served only as a check.

Gallenne et al. (2018), as part of their investigation into red-clump stars, also spent time confirming the wavelength scale of PIONIER using a different approach: through spectral calibration in conjunction with the second generation VLTI instrument GRAVITY (Eisenhauer et al. 2011). Through interleaved observations with both instruments over two half nights of the previously characterized binary TZ For (Gallenne et al. 2016), they studied the orbital separation of the binary, taking advantage of GRAVITY's internal laser reference source (accurate to < 0.02 per cent) for calibration. Combining data they found a relative difference of 0.35 per cent in the measured separations, consistent with Kervella et al. (2017), which was taken to be the systematic uncertainty of the PIONIER wavelength calibration. The authors do not report a *systematic* offset equivalent to γ from Kervella et al. (2017), only a relative uncertainty, with subsequent work involving authors of both investigations using only this relative value (Gallenne et al. 2019).

Lachaume et al. (2019), and the associated Rabus et al. (2019), undertook investigation into the statistical uncertainties and systematics when using PIONIER to measure diameters for underresolved low-mass stars. They make use of the findings of Gallenne et al. (2018) and take the uncertainty on the central wavelength of each spectral channel, and thus the spatial frequency itself, to be ± 0.35 per cent. Rather than applying this uncertainty to the x-axis spatial frequency values during modelling, they instead translate the error to a y-axis uncertainty in visibility. During modelling, the uncertainties are sampled and treated as a correlated systematic source of error for all observations taken on a single night with the same configuration, and uncorrelated otherwise.

With these recent results in mind, the wavelength calibration strategy for this work is to use the spectral dispersion information calibration available on each night, and adopt an uncertainty of 0.35 per cent on our wavelength scale per the conclusions of Kervella et al. (2017) and Gallenne et al. (2018). Following the approach of subsequent investigations (Gallenne et al. 2019; Lachaume et al. 2019; Rabus et al. 2019), we do not consider a systematic offset in the wavelength scale. For the results described here, this relative uncertainty is added in quadrature with all bootstrapped angular diameter uncertainties.

2.5 Data reduction

A single CAL-SCI-CAL-SCI-CAL sequence generates five interferogram and a single dark exposure per target (each consisting of 100 scans), plus a set of flux splitting calibration files known as a 'kappa matrix' (consisting of four files, each with a separate telescope shutter open). This produces 34 files per observational sequence, though this can be more in practice if more observations are required to replace those of poor quality. This raw data can be accessed and downloaded in bulk through the ESO archive.[4]

PNDRS[5] Bouquin et al. (2011), the standard PIONIER data-reduction pipeline, was used to go from raw data to calibrated squared visibility (V^2) measurements of our science targets. During reduction the exposures are averaged together, to produce 36 V^2 points for each of the two science target observation (six wavelength channels on six independent baselines), resulting in 72 V^2 points for the entire sequence. PNDRS uses the calibrators in the bracketed sequence to determine the instrumental and atmospheric transfer function by interpolating in time.

The PYTHON package REACH,[6] written for this project, was used to interface with PNDRS to perform simple tasks such as providing files of calibrator estimated diameters, and using the standard PNDRS script reading functionality to exclude bad calibrators (e.g. binaries) or baselines (e.g. lost tracking) from being using for calibration. REACH also exists to perform the more complex task of accurate V^2 uncertainty estimation considering correlated or non-Gaussian errors. Similar to the approach of Lachaume, Rabus & Jordán (2014) and Lachaume et al. (2019), we perform a bootstrapping algorithm on the calibrated interferograms within each given CAL-SCI-CAL-SCI-CAL sequence, in combination with Monte Carlo sampling of the predicted calibrator angular diameters, and science target stellar parameters ($T_{\rm eff}$, log g, and [Fe/H]) and magnitudes, for calculation of limb darkening coefficients, bolometric fluxes (see Sections 3.1–3.5), radii, and luminosities.

Our bootstrapping implementation samples (with repeats) the five interferograms of each science or calibrator target in the sequence independently, rather than sampling from the combined 10 science and 15 calibrator interferograms, respectively. In addition, predicted calibrator angular diameters are sampled at each step from a normal distribution using the uncertainties on the colour–angular diameter relations. The results as presented here were bootstrapped 5000 times, fitting for both $\theta_{\rm UD,\,sci}$ and $\theta_{\rm LD,\,sci}$, and calculating $f_{\rm bol}$, $T_{\rm eff}$, radius (R), and luminosity (L) once per iteration. Final values for each parameter, as well as each ${V_{\rm tar,\,corrected}}^2$ point (for the plots in Fig. 2), and their uncertainties were calculated through the mean and standard deviations of the resulting probability distributions. The Monte Carlo/diameter fitting process was then completed once more in its entirety, but sampling our interferometry derived $T_{\rm eff}$ values in place of their literature equivalents from Table 1. The effect of this is for our limb darkening coefficients and bolometric fluxes to be sampled with less scatter by using values with smaller and more consistent uncertainties, in effect 'converging' to the final reported values in Table 4.

3 RESULTS

3.1 Limb darkened angular diameters

A linearly limb darkened disc model is a poor fit to both real and model stellar atmospheres, but in order to properly resolve the intensity profile and take advantage of higher order limb darkening laws (e.g. equation 5 below, from Claret 2000), one must resolve beyond the first lobe of the visibility profile:

$$\frac{I(\mu)}{I(1)} = 1 - \sum_{k=1}^{4} a_k (1 - \mu^{\frac{k}{2}}), \tag{5}$$

where $I(1)$ is the specific intensity at the centre of the stellar disc, $\mu = \cos(\gamma)$ with angle γ between the line of sight and emergent intensity, k the polynomial order, and a_k the associated coefficient.

In the first and second lobes, the visibilities of a 4-term limb darkening law are nearly indistinguishable from linearly darkened model of slightly different diameter and appropriate coefficient. We thus model the intensity profile with a four term law, interpolating the 3D STAGGER grid of model atmospheres (Magic, Weiss &

[4] http://archive.eso.org/cms.html
[5] http://www.jmmc.fr/data_processing_pionier.htm
[6] https://github.com/adrains/reach

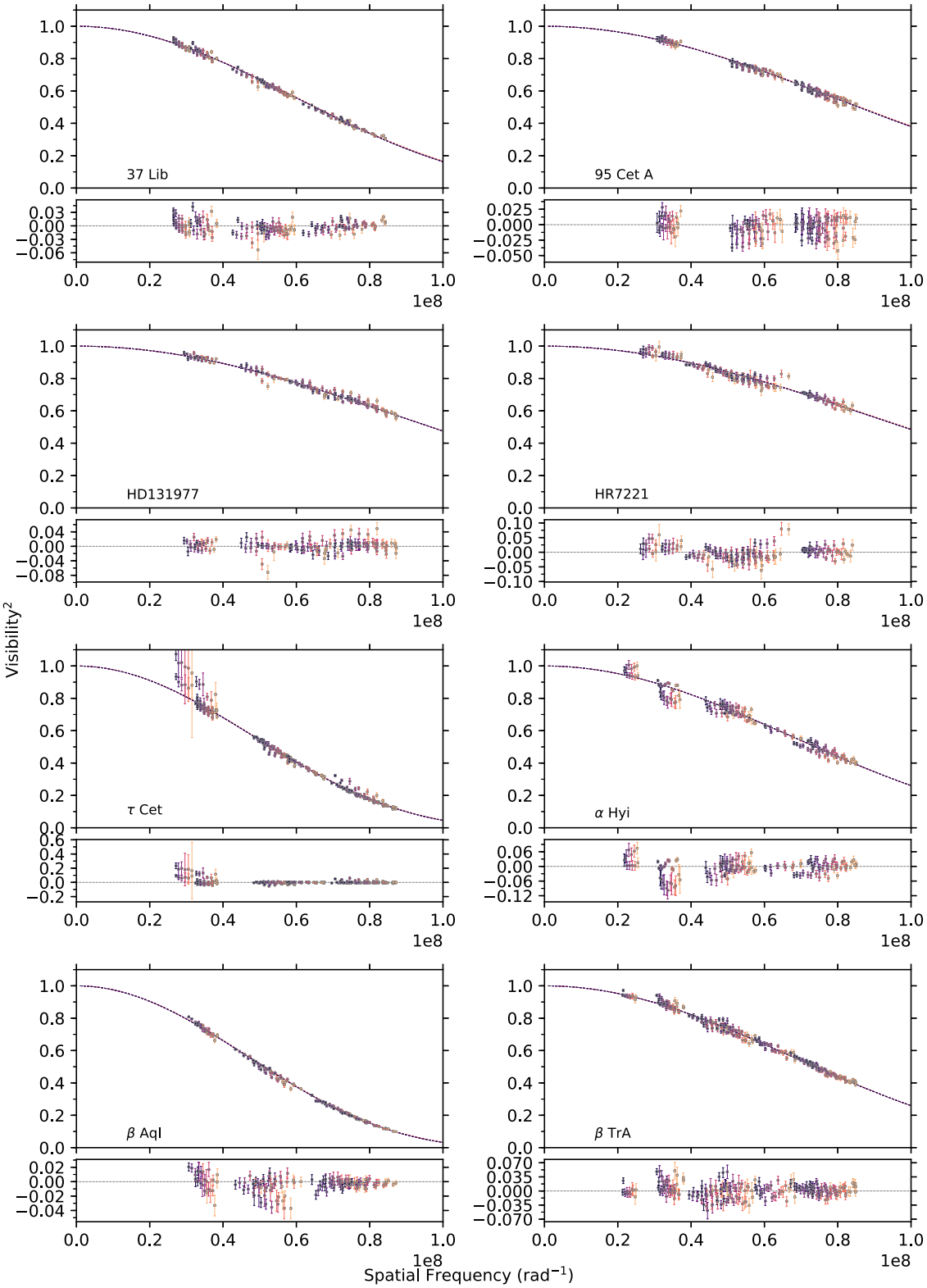

Figure 2. V^2 fits using final means and standard deviations from bootstrapped distributions. Point colour corresponds to one of the six PIONIER wavelength channels, with darker points being redder wavelengths.

Asplund 2015) initially with the $T_{\rm eff}$, $\log g$, and [Fe/H] given in Table 1, then a second and final time using the resulting estimate of the interferometric $T_{\rm eff}$. Note that STAGGER assumes $v \sin i = 0$ km s^{-1}, however, the fastest rotating stars in our sample are too hot for the grid (discussed below), minimizing the influence of this limitation.

For the results presented here, obtained at the highest resolution possible at the VLTI, we resolve only the first lobe for all stars

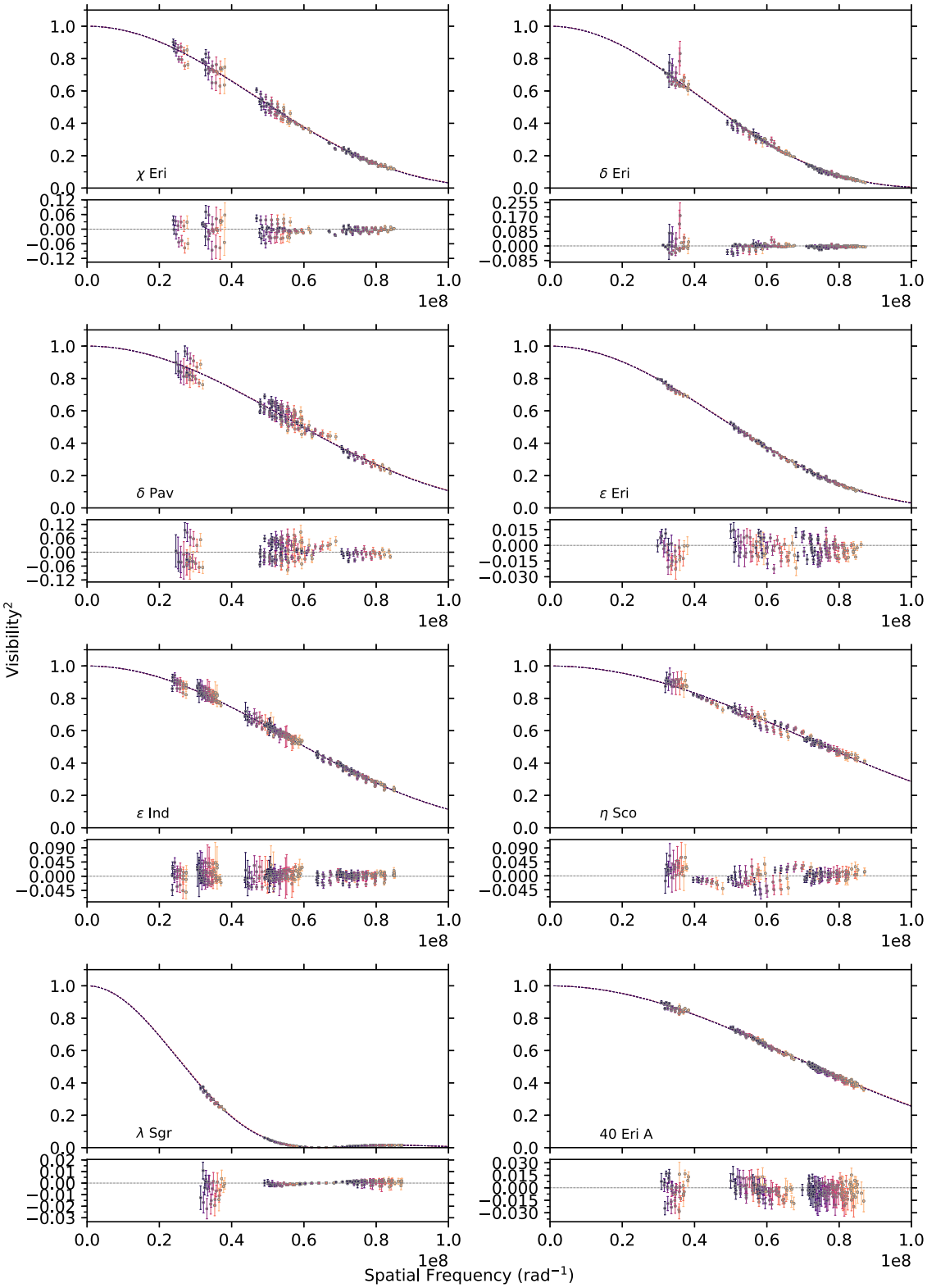

Figure 2 – *continued*

bar λ Sgr (see Section 3.2). This means that we do not resolve the intensity profile well enough to take full advantage of higher order polynomial limb darkening laws. Given this limitation, the best approach, which can be considered analogous to reducing the resolution of the model to the resolution of the data available, would be an equivalent linear coefficient to the four term model described above. The so called 'equivalent linear coefficient' is the coefficient that gives the same side-lobe height for both models, though with a

slightly smaller value of $\theta_{\rm LD}$ of the order 0.4–0.5 per cent, corrected for by the scaling factor s_λ. This is formalized in White et al. (in preparation).

For each target, we fitted a modified linearly limb darkened disc model per Hanbury Brown et al. (1974):

$$V^2 = C\left(\left(\frac{1-u_\lambda}{2}+\frac{u_\lambda}{3}\right)^{-1}\left[(1-u_\lambda)\frac{J_1(x)}{x}+u_\lambda(\pi/2)^{1/2}\frac{J_{3/2}(x)}{x^{3/2}}\right]\right)^2 \quad (6)$$

with

$$x = \pi B s_\lambda \theta_{\rm LD}\lambda^{-1}, \quad (7)$$

where V is the calibrated fringe visibility, C is an intercept scaling term, u_λ is the wavelength dependent linear limb darkening coefficient, s_λ the wavelength dependent diameter scaling term, $J_n(x)$ is the nth order Bessel function of the first kind, B is the projected baseline, and λ is the observational wavelength. Fitting was performed using `scipy`'s *fmin* minimization routine with a χ^2 loss function.

The intercept term C, and diameter scaling parameter s_λ, are the sole modifications to the standard linearly darkened disc law. In the ideal case where all calibrators are optimal and the system transfer function is estimated perfectly, C would not be required as the calibrated visibilities would never be greater than 1. With non-ideal calibrators however, the calibration is imperfect and this is no longer the case. Deviations from $V^2 \leq 1$ are generally small, but in the case of our bright science targets with faint calibrators, PNDRS had significant calibration issues, something discussed further in Section 3.3. Thus whilst the fitting was done simultaneously on data from all sequences, each sequence of data was fit with a separate value of C. We also fit for the uniform disc diameter $\theta_{\rm UD}$ using equation (6), but set $u_\lambda = 0$ for the case of no limb darkening.

Usage of the STAGGER grid also confers another advantage: the ability to compute u_λ for each wavelength channel of PIONIER, rather than the grid being defined broadly for the entire H band as in Claret & Bloemen (2011). Thus when fitting equation (6), u_λ is actually a vector of length 6 – one for each of the PIONIER wavelength channels ($\lambda \approx$ 1.533, 1.581, 1.629, 1.677, 1.7258, 1.773 μm). STAGGER however covers a limited parameter space, with the coolest stars in our sample (ϵ Ind, HD 131977), and the hottest (α Hyi, η Sco, β Aql), falling outside the grid bounds. For these stars, the grid of Claret & Bloemen (2011) is interpolated (with microturbulent velocity of 2 km s^{-1}) for the sampled parameters and used instead, which in practice means $u_{\lambda,\,1-6}$ are identical, and $s_{\lambda,\,1-6} = 1.0$. Table C1 quantifies the difference in $\theta_{\rm LD}$ obtained using each of these two approaches.

Fig. 2 shows V^2 fits for each of our science targets, with point colour corresponding to the observational wavelength (where darker points correspond to redder wavelengths). Note that fitting for both $\theta_{\rm UD}$ and $\theta_{\rm LD}$ was done once per bootstrapping iteration, such that these plots use the mean and standard deviations of the final distributions for each V^2 point, C, u_λ, s_λ, and $\theta_{\rm LD}$. To aid readability by showing only a single diameter fit for each star, each sequence of data has been normalized by its corresponding value of C.

Final values for $\theta_{\rm UD}$ and $\theta_{\rm LD}$ fits, with the systematic uncertainty of PIONIER's wavelength scale added in quadrature, are presented in Table 4, and adopted u_λ and s_λ in Table C2.

3.2 Limb darkening of λ Sgr

Fig. 3 shows a zoomed in plot of the λ Sgr fit, focusing on the resolved sidelobe. Comparing the model fits to the uniform disc

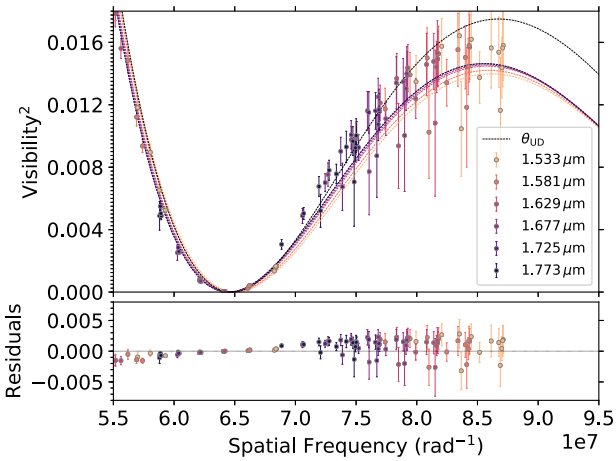

Figure 3. Zoomed in view of λ Sgr sidelobe and limb darkening effects.

curve, the effect of limb darkening is clear. However, with only a single star from our sample being this well resolved, it is difficult to comment on whether the observed limb darkening is consistent with models. Using PIONIER Kervella et al. (2017) found their α Centauri A and B results to be significantly less limb darkened than both 1D and 3D model atmosphere predictions. A similar investigation at the CHARA Array is ongoing, with results to be published as White et al. (in preparation).

3.3 Transfer function calibration

In the case of perfect calibration, that is to say the influence of the system transfer function on the measured visibilities has been entirely removed, V^2 should be $0 \leq V^2 \leq 1$ and consistent with a limb darkened disc model for single stars. For many of our sequences, this was not the case, resulting in significant calibration issues where measured V^2 was systematically higher than the model, necessitating our modification of the intercept for the standard linear limb darkening law in equation (6).

Table 3 shows the best-fitting intercept parameter for each observational sequence, where every star in a given sequence was observed with the same integration time. Recalling that *bright* sequences were those preferencing similarity in science and calibrator target magnitudes, and *faint* sequences were those prioritizing science-calibrator on-sky separation, our mean C values are as follows: $C_{\rm bright} = 1.04 \pm 0.03$, $C_{\rm faint} = 1.05 \pm 0.03$. This difference is marginal, but is not without precedent (as discussed below), and indeed non-linear behaviour at high visibility due to the difference in brightness between science and calibrator is a known, if unaddressed, issue with PIONIER.

Wittkowski et al. (2017) encountered high V^2 at short baselines, systematically above model predictions, when imaging both the carbon AGB star R Scl ($H \sim 0.49$), and the nearby resolved K5/M0 giant υ Cet ($H \sim 0.27$) for comparison and validation. Both targets were observed with the same selection of calibrators: HD 6629 ($H \sim 2.90$), HR 400 ($H \sim 1.85$), ξ Scl ($H \sim 2.65$), HD 8887 ($H \sim 4.29$), HD 9961 ($H \sim 3.91$), HD 8294 ($H \sim 4.36$), and HR 453 ($H \sim 3.72$), on average being nearly three magnitudes fainter than the science and check targets. They conclude the systematic as being most likely caused by either this difference in magnitude or air masses between the science and calibrator targets, and took it into account by excluding the short baseline V^2 data during modelling and image synthesis.

Table 3. Fitted intercept parameter C for each observational sequence.

Star	Period	Sequence	C_{LD}	C_{UD}
37 Lib	99	Bright	1.007 ± 0.007	1.006 ± 0.007
37 Lib	99	Faint	1.045 ± 0.006	1.045 ± 0.006
95 Cet A	99	Bright	1.028 ± 0.010	1.027 ± 0.010
95 Cet A	99	Faint	1.064 ± 0.006	1.063 ± 0.006
HD131977	101	Bright	1.009 ± 0.007	1.009 ± 0.007
HD131977	101	Faint	1.034 ± 0.009	1.034 ± 0.009
HR7221	101	Bright	1.032 ± 0.008	1.031 ± 0.008
HR7221	101	Faint	1.010 ± 0.007	1.009 ± 0.007
τ Cet	99	Bright	1.021 ± 0.013	1.018 ± 0.013
τ Cet	101	Bright	1.067 ± 0.012	1.064 ± 0.012
τ Cet	99	Faint	1.108 ± 0.014	1.105 ± 0.014
τ Cet	101	Faint	1.072 ± 0.011	1.070 ± 0.011
α Hyi	99	Bright	1.044 ± 0.008	1.043 ± 0.008
α Hyi	99	Faint	1.016 ± 0.018	1.015 ± 0.018
β Aql	101	Bright	1.017 ± 0.008	1.014 ± 0.008
β Aql	101	Faint	1.051 ± 0.010	1.048 ± 0.010
β TrA	99	Bright	1.064 ± 0.010	1.064 ± 0.010
β TrA	101	Bright	1.090 ± 0.007	1.089 ± 0.007
β TrA	101	Faint	1.041 ± 0.009	1.040 ± 0.009
χ Eri	99	Bright	1.090 ± 0.022	1.087 ± 0.022
χ Eri	99	faint	1.073 ± 0.009	1.070 ± 0.009
δ Eri	102	bright	1.091 ± 0.023	1.084 ± 0.023
δ Eri	99	Faint	1.055 ± 0.006	1.050 ± 0.006
δ Eri	102	Faint	1.020 ± 0.005	1.015 ± 0.005
δ Pav	99	Bright	1.049 ± 0.022	1.048 ± 0.022
δ Pav	99	Faint	1.018 ± 0.029	1.017 ± 0.029
ϵ Eri	99	Bright	1.011 ± 0.008	1.008 ± 0.008
ϵ Eri	99	Faint	1.049 ± 0.008	1.046 ± 0.008
ϵ Ind	99	Bright	1.004 ± 0.008	1.003 ± 0.008
ϵ Ind	101	Bright	1.043 ± 0.009	1.042 ± 0.009
ϵ Ind	99	Faint	1.080 ± 0.024	1.079 ± 0.024
ϵ Ind	101	Faint	1.005 ± 0.008	1.003 ± 0.008
η Sco	101	Bright	1.061 ± 0.010	1.060 ± 0.010
η Sco	101	Faint	1.169 ± 0.029	1.169 ± 0.029
λ Sgr	99	Bright	1.029 ± 0.027	0.994 ± 0.027
λ Sgr	99	Faint	1.036 ± 0.022	1.003 ± 0.023
40 Eri A	102	Bright	0.998 ± 0.011	0.997 ± 0.011
40 Eri A	99	Faint	1.078 ± 0.006	1.077 ± 0.006
40 Eri A	102	Faint	1.045 ± 0.005	1.043 ± 0.005

Observations to image granulation on π Gru ($H \sim -1.71$) in Paladini et al. (2018) were also subject to the same systematic. The two calibrators used, HD 209688 ($H \sim 1.44$) and HD 215104 ($H \sim 2.61$), were both substantially fainter than the science target by $\geq$3 mag. The authors do not go into detail about how they addressed the miscalibration other than adding a flat 5 per cent systematic relative uncertainty to their data.

The corresponding mean difference between our science target and 'good' (i.e. used) calibrator magnitudes in H is $\Delta H_{\rm bright} = 0.95$, and $\Delta H_{\rm faint} = 1.69$. If the issue indeed stems from ΔH being large, then the marginal difference we observe in C is at least consistent with the bright sequences on average having a lower ΔH.

3.4 Bolometric fluxes

Determination of $T_{\rm eff}$ requires measurement of $f_{\rm bol}$, the bolometric flux received at Earth, which can be done through one of several techniques, each with precedent in optical interferometry literature. All are only accurate to the few per cent level, primarily due to uncertainties on the adopted zero-points used to convert fluxes, either real or synthetic, to magnitudes and vice versa.

The least model dependent approach is to use a combination of spectrophotometry and broad-band photometry from the science target itself, in combination with synthetic equivalents for missing or contaminated regions, to construct the flux-calibrated spectral energy distribution of the star from which $f_{\rm bol}$ can be determined. White et al. (2018) implemented this procedure, using the methodology outlined in Mann et al. (2015).

A related technique is to employ a library of flux-calibrated template spectra covering a range of spectral types, e.g. the *Pickles Atlas* (115–2500 nm, Pickles 1998), in lieu of spectrophotometry from the targets themselves. Fits are then performed to target broad-band photometry using library spectra of adjacent spectral types. This was the approach taken by e.g. van Belle, Ciardi & Boden (2007), van Belle et al. (2008), Boyajian et al. (2012a, b, 2013), and White et al. (2013), which lacks the limitations associated with synthetic spectra (e.g. due to modelling assumptions such as one-dimensional and hydrostatic models, or models satisfying local thermodynamic equilibrium). However, it is limited in its use of a relatively coarse, non-interpolated grid of only 131 spectra of mostly Solar metallicity, with potential errors from reddened spectra and correlated errors associated with the photometric calibration.

In lieu of a template library, the previous approach can be conducted using a grid of purely synthetic spectra. By linearly interpolating the spectral grid in $T_{\rm eff}$, $\log g$, and [Fe/H] and fitting to available broad-band photometry, $f_{\rm bol}$ can be determined as the total flux from the best-fitting spectrum. This was the method employed by Rabus et al. (2019), who used PHOENIX model atmospheres (Husser et al. 2013), assuming [Fe/H] = 0 for all targets (likely to avoid degeneracies between $T_{\rm eff}$ and [Fe/H] for cool star spectra), as well as Huber et al. (2012) using the MARCS grid of model atmospheres (Gustafsson et al. 2008). This technique has the advantage of being unaffected by instrumental or atmospheric effects, and allowing for a much finer grid, but makes the results more susceptible to potential inaccuracies within the models themselves. We note however that synthetic photometry from the MARCS grid has previously been shown to be valid using the colours from both globular and open clusters, across the HR diagram and over a wide range of metallicities ($-2.4 \lesssim$ [Fe/H] $\lesssim +0.3$, Brasseur et al. 2010; VandenBerg, Casagrande & Stetson 2010).

The final approach to be discussed here, and the one employed for this work, computes $f_{\rm bol}$ using broad-band photometry and the appropriate bolometric correction derived from model atmospheres using literature values of $T_{\rm eff}$, $\log g$, and [Fe/H]. This method saw use in Karovicova et al. (2018), and in White et al. (2018) who found it to have excellent consistency with results derived from pure spectrophotometry for all but one of their stars. Casagrande & VandenBerg (2018b) evaluated the validity of using bolometric corrections in this manner by comparing results to the $\sim$1 per cent precision CALSPEC library (Bohlin 2007) of *Hubble Space Telescope* spectrophotometry. This demonstrated that bolometric fluxes could be recovered from computed bolometric corrections to the 2 per cent level, a value typically halved when combining the results from more photometric bands (as we do here, corresponding to roughly $\pm$12.5 K uncertainty on $T_{\rm eff}$ for a 5000 K star with a 1 per cent error on flux).

Given that all have been demonstrated successfully in the literature, we opt for the bolometric correction technique because of limited available well-calibrated photometry for our bright targets. Bolometric fluxes were computed for all stars by way of the

Table 4. Final fundamental stellar parameters.

Star	$\theta_{\rm UD}$ (mas)	$\theta_{\rm LD}$ (mas)	R ($R_\odot$)	$f_{\rm bol}$ (10^{-8} erg s^{-1} cm^{-2})	$T_{\rm eff}$ (K)	L ($L_\odot$)
τ Cet	2.005 ± 0.011	2.054 ± 0.011	0.796 ± 0.004	115.0 ± 1.2	5347 ± 18	0.47 ± 0.01
α Hyi	1.436 ± 0.016	1.460 ± 0.016	3.040 ± 0.058	179.0 ± 3.0	7087 ± 47	21.00 ± 0.75
χ Eri	2.079 ± 0.011	2.134 ± 0.011	3.993 ± 0.027	104.0 ± 4.0	5115 ± 49	9.84 ± 0.39
95 Cet A	1.244 ± 0.012	1.280 ± 0.012	8.763 ± 0.128	26.2 ± 1.7	4678 ± 75	33.18 ± 2.27
ϵ Eri	2.087 ± 0.011	2.144 ± 0.011	0.738 ± 0.003	99.8 ± 2.5	5052 ± 33	0.32 ± 0.01
δ Eri	2.343 ± 0.009	2.411 ± 0.009	2.350 ± 0.010	123.2 ± 3.4	5022 ± 34	3.17 ± 0.09
40 Eri A	1.449 ± 0.012	1.486 ± 0.012	0.804 ± 0.006	50.8 ± 0.9	5126 ± 30	0.40 ± 0.01
37 Lib	1.639 ± 0.009	1.684 ± 0.010	5.133 ± 0.043	50.6 ± 2.6	4809 ± 62	12.71 ± 0.69
β TrA	1.438 ± 0.013	1.462 ± 0.013	1.976 ± 0.021	188.2 ± 2.1	7171 ± 35	9.30 ± 0.17
λ Sgr	3.910 ± 0.014	4.060 ± 0.015	11.234 ± 0.181	283.9 ± 8.7	4768 ± 36	58.79 ± 2.61
δ Pav	1.785 ± 0.025	1.828 ± 0.025	1.197 ± 0.016	107.2 ± 2.5	5571 ± 48	1.24 ± 0.03
ϵ Ind	1.758 ± 0.012	1.817 ± 0.013	0.711 ± 0.005	51.5 ± 3.7	4649 ± 84	0.21 ± 0.02
HD131977	1.098 ± 0.014	1.130 ± 0.014	0.715 ± 0.009	17.6 ± 1.1	4505 ± 76	0.19 ± 0.01
η Sco	1.392 ± 0.017	1.416 ± 0.017	3.307 ± 0.050	121.6 ± 2.0	6533 ± 46	17.94 ± 0.45
β Aql	2.079 ± 0.011	2.133 ± 0.012	3.064 ± 0.020	100.3 ± 2.9	5071 ± 37	5.60 ± 0.17
HR7221	1.088 ± 0.014	1.117 ± 0.015	4.428 ± 0.058	26.5 ± 0.7	5023 ± 47	11.24 ± 0.33

BOLOMETRIC-CORRECTIONS[7] software (Casagrande & VandenBerg 2014, 2018b; Casagrande et al. 2018). For a given set of $T_{\rm eff}$, $\log g$, and [Fe/H] the software produces synthetic bolometric corrections in different filters by interpolating the MARCS grid of synthetic spectra (Gustafsson et al. 2008). $f_{\rm bol}$ is obtained using equation (8) (Casagrande & VandenBerg 2018b):

$$f_{\rm bol} = \frac{\pi L_\odot}{1.296 \times 10^9 \text{ au}} 10^{-0.4(\mathrm{BC}_\zeta - M_{\rm bol,\odot} + m_\zeta - 10)}, \quad (8)$$

where $f_{\rm bol}$ is the stellar bolometric flux received at Earth in erg s^{-1} cm^{-2}, $L_\odot$ is the Solar bolometric luminosity in erg s^{-1} (IAU 2015 Resolution B3, 3.828×8^{33} erg s^{-1}cm^{-2}), au is the astronomical unit (IAU 2012 Resolution B2, $1.495978707 \times 10^{13}$ cm), BC_ζ and m_ζ are the bolometric correction and apparent magnitudes, respectively, in filter band ζ, and $M_{\rm bol} = 4.75$ is the adopted Solar bolometric magnitude.

Calculation of $f_{\rm bol,\,\zeta}$ is done at each iteration of the aforementioned bootstrapping and Monte Carlo algorithm for each of $H_{\rm P}$, $B_{\rm T}$, and $V_{\rm T}$ filter bands using the sampled stellar parameters and magnitudes, overwhelmingly consistent to within 1σ uncertainties. An instantaneous value of $f_{\rm bol,\,final}$ is calculated by averaging the fluxes obtained from each filter, with final values obtained as the mean and standard deviation of the respective distributions. Note that, with the goal of consistency in mind, *Gaia* G, $B_{\rm P}$, and $R_{\rm P}$ were avoided due to saturation for a portion of our sample (and a magnitude-dependent offset for bright targets as noted in Casagrande & VandenBerg 2018a).

The final calculated bolometric fluxes for each band are reported in Table B1 and visualized in Fig. B1, with the adopted average values in Table 4.

3.5 Fundamental stellar properties

The strength of measuring stellar angular diameters through interferometry is the ability to measure $T_{\rm eff}$ independent of distance in an almost entirely model independent way (the exceptions being the adopted limb darkening law, and ∼1 per cent precision bolometric fluxes). With measures of stellar angular diameter and flux, $T_{\rm eff}$ can be calculated as follows:

$$T_{\rm eff} = \left(\frac{4 f_{\rm bol}}{\sigma \theta_{\rm LD}{}^2} \right)^{1/4}, \quad (9)$$

where $T_{\rm eff}$ is the stellar effective temperature in K, $f_{\rm bol}$ is the bolometric stellar flux in erg s^{-1} cm^{-2}, and σ is the Stefan–Boltzmann constant, taken to be $\sigma = 5.6704 \times 10^{-5}$ erg s^{-1} cm^{-2} K^{-4}.

The same measure of flux can be combined with the distance to the star to calculate the bolometric luminosity:

$$L = 4\pi f_{\rm bol} D^2, \quad (10)$$

where D is again the distance to the star. Dividing this value by $L_\odot$ gives the luminosity in Solar units.

Finally, the measured angular diameter and distance can be combined to determine the physical radius of a star:

$$R = \frac{1}{2} \theta_{\rm LD} D \quad (11)$$

and its uncertainty:

$$\sigma_R = R \sqrt{ \left(\frac{\sigma_\theta}{\theta_{\rm LD}} \right)^2 + \left(\frac{\sigma_D}{D} \right)^2 }, \quad (12)$$

where R is the physical radius of the star, $\theta_{\rm LD}$ is the limb darkened angular diameter, D is the distance to the star, and σ_θ and σ_D are their respective uncertainties. These can be put into Solar units using pc $= 3.0857 \times 10^{13}$ km, and $R_\odot = 6.957 \times 10^5$ km.

These parameters, alongside the final angular diameters, are reported in Table 4.

4 DISCUSSION

4.1 Comparison with previous interferometric measurements

Six of our samples, HD 131977, 40 Eri A, ϵ Ind, τ Ceti, β Aql, and ϵ Eri, have literature angular diameter measurements (Table 5), which we find to be consistent with our own to within $\sim 1\sigma$ uncertainties for all but one star (Fig. 4). Our value for ϵ Ind however is substantially discrepant to the VINCI diameter by $\sim 4\sigma$. Comparing our V^2 fits to the literature results in Demory et al. (2009) reveals that we place

[7] https://github.com/casaluca/bolometric-corrections

Table 5. Comparison of angular diameters reported here with stars measured previously in the literature.

Star	θ_{LD} (mas)	Facility	Instrument	Refs.
τ Cet	1.971 ± 0.05	VLTI	VINCI	1
	2.078 ± 0.031	VLTI	VINCI	2
	2.015 ± 0.011	CHARA	FLUOR	3
ϵ Eri	2.148 ± 0.029	VLTI	VINCI	2
	2.126 ± 0.014	CHARA	FLUOR	3
	2.153 ± 0.028	NPOI	NPOI	4
40 Eri A	1.437 ± 0.039	VLTI	AMBER	5
ϵ Ind	1.881 ± 0.017	VLTI	VINCI	5
HD131977	1.177 ± 0.029	VLTI	VINCI	5
β Aql	2.18 ± 0.09	NPOI	NPOI	6

Notes. References. 1. Pijpers et al. (2003); 2. Di Folco et al. (2004); 3. di Folco et al. (2007); 4. Baines & Armstrong (2012); 5. Demory et al. (2009); 6. Nordgren et al. (1999)

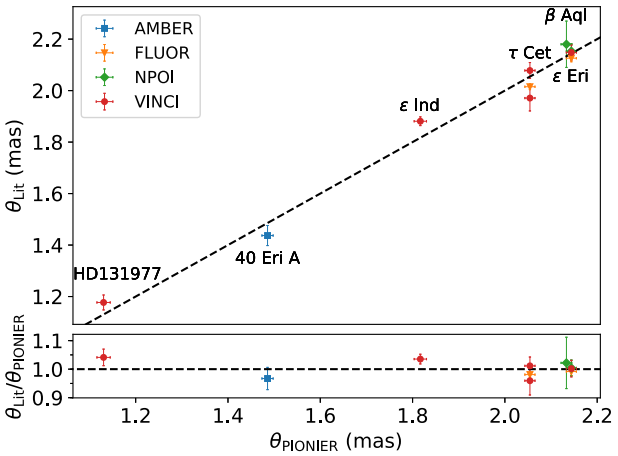

Figure 4. Comparison of PIONIER diameters as reported here, to stars with literature measurements from other interferometers or beam-combiners.

tighter constraints on the angular diameter by better resolving the star down to V^2 of ∼0.2 versus ∼0.5 for previous results. We expect the discrepancy is largely caused by this, plus the fact that these observations were taken at lower sensitivity using two 35 cm test siderostats during the early years of the VLTI rather than the four 1.8 m ATs we have access to now.

None of these prior measurements were made with PIONIER, meaning that our results offer high-precision agreement between not only different VLTI beam combiners (AMBER and VINCI), but also as different facilities altogether (NPOI[8] and CHARA/FLUOR). Given the relatively sparse overlaps however, we are not able to say anything substantial about potential systematics. We await the upcoming White et al. (in preparation) which will be able to compare PIONIER to CHARA/PAVO for τ Cet, ϵ Eri, δ Eri, 37 Lib, and β Aql. This study will also possibly enable the ability to investigate the effect of limb darkening at different wavelengths since PAVO is an *R*-band instrument, thus significantly improving the sensitivity to systematic errors. Furthermore, PAVO data not only for additional dwarf and giant stars, including β Aql, but also for many stars not observed here, are to be published soon in Karovicova et al. (in preparation) and a following series of papers.

[8]Note that for simplicity NPOI is used here to refer to both the *Navy Prototype Optical Interferometer* (per Nordgren et al. 1999) and the *Navy Optical Interferometer* (per Baines & Armstrong 2012) given the facility changed names between the two measurements referenced here, and is now known as the *Navy Precision Optical Interferometer*.

4.2 Comparison with colour–θ_{LD} relations

Fig. 5 shows a comparison between our fitted diameters, and the $(V - W3)$, $(V - W4)$, and the [Fe/H] dependent $(B - V)$ colour–θ_{LD} relations from Boyajian et al. (2014) used to predict calibrator angular diameters. All three sets of relations are consistent within errors with our results (despite several of our sample being marginally too red for the [Fe/H] dependent $(B - V)$ relation), which bodes well for the accuracy of the relations. However, there appears a clear systematic offset for the $(V - W3)$ relation, plus a less severe offset for the $(V - W4)$ relation. There does not appear to be a trend in either [Fe/H] with any of these relations.

4.3 T_{eff} from empirical relations

Unfortunately comparison of the T_{eff} values derived here to those from IR Flux method (Casagrande et al. 2010) is not possible due to saturated *2MASS* photometry – the critical source of infrared photometry. Another source of comparison is to use the empirical relations provided by the same study, which give an empirical mapping between select colour indices and T_{eff}. Fig. 6 presents T_{eff} as a function of $(B_T - V_T)$, uncertainties ±79 K, and demonstrates 1σ agreement for all stars, with the exceptions of HD 131977 and β TrA. Inspecting the photometry for both stars, values of f_{bol} derived from different filter bands are consistent, and rotation does not appear to be a significant factor when considering literature $v \sin i$ presented in Table 1. We note however that our interferometric temperatures are consistent with the literature spectroscopic values also listed in Table 1 for these two stars.

5 CONCLUSIONS

We have used long-baseline optical interferometry to measure the angular diameters for a sample of 16 southern stars (6 dwarf, 5 subgiant, and 5 giants) with exquisite precision using the PIONIER instrument on the VLTI. The limb darkened diameters reported have a mean uncertainty of ∼ 0.82 per cent, and were obtained using a robust calibration strategy, and a data analysis pipeline implementing both bootstrapping and Monte Carlo sampling to take into account correlated uncertainties in the interferometric data. In addition to this, we also report derived T_{eff}, physical radii, bolometric fluxes, and luminosities for all stars, with mean uncertainties of ∼ 0.9 per cent, ∼ 1.0 per cent, ∼ 3.3 per cent, and ∼ 3.7 per cent respectively.

Ten of these stars did not have measured angular diameters prior to the results presented here, and the majority of the remaining six have values in agreement with previous literature measurements, with the sole outlier being observed at higher resolution and with greater sensitivity here. These are some of the closest and most well-studied stars, and this work hopes to elevate them further to the level of spectral type standards, where they can provide constraints to theoretical models and empirical relations.

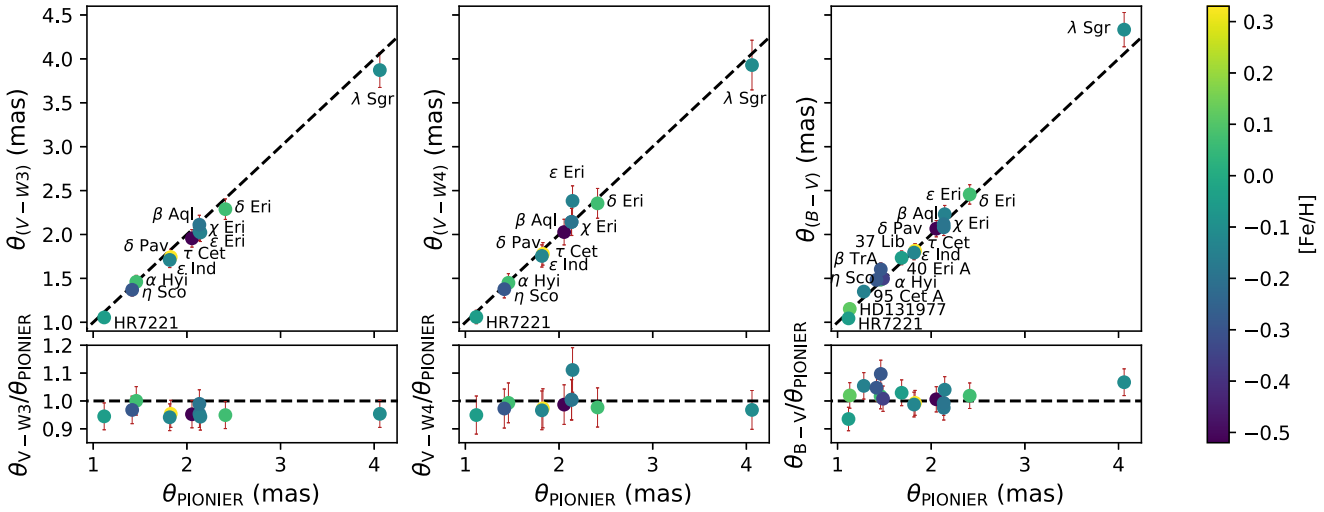

Figure 5. Comparison of θ_{LD} as reported here as compared to predicted diameters from Boyajian et al. (2014). *Left:* $(V - W3)$ relation, *Centre:* $(V - W4)$ relation, *Right:* [Fe/H] dependent $(B - V)$ relation. Note that not all stars have *WISE* photometry, whereas all stars have available *Tycho-2* magnitudes.

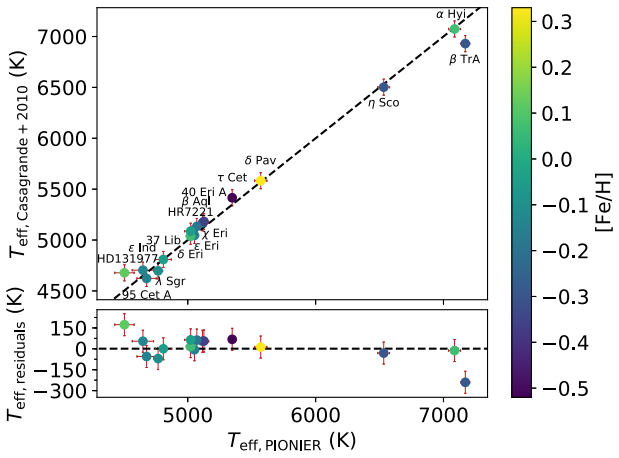

Figure 6. Comparison of T_{eff} as reported here and those calculated from $(B_T - V_T)$ using the empirical relations of Casagrande et al. (2010).

ACKNOWLEDGEMENTS

ADR acknowledges support from the Australian Government Research Training Program, and the Research School of Astronomy & Astrophysics top up scholarship. We acknowledge Australian Research Council funding support through grants DP170102233. LC is the recipient of an Australian Research Council Future Fellowship (project number FT160100402). Based on observations obtained under European Southern Observatory (ESO) program IDs 099.D-2031(A), 0101.D-0529(A), and 0102.D-0562(A). This research has made use of the `PIONIER data reduction package` of the Jean-Marie Mariotti Center.[9] This research has made use of the *Washington Double Star Catalog* maintained at the U.S. Naval Observatory. This work made use of the *SIMBAD* and *VIZIER* astrophysical database from CDS, Strasbourg, France and the bibliographic information from the National Aeronautics and Space Administration (NASA) Astrophysics Data System. We thank the anonymous referee for their helpful comments.

Software: `ASTROPY` (Astropy Collaboration et al. 2013), `NUMPY` (Oliphant 2006), `SCIPY` (Jones, Oliphant & Peterson 2016), `IPYTHON` (Perez & Granger 2007), `PANDAS` (McKinney 2010), and `MATPLOTLIB` (Hunter 2007).

[9]Available at http://www.jmmc.fr/pionier

REFERENCES

Allende Prieto C., Barklem P. S., Lambert D. L., Cunha K., 2004, A&A, 420, 183
Allende Prieto C. et al., 2008, Astron. Nachr., 329, 1018
Aller L. H. et al., 1982, Landolt-Bornstein: Numerical Data and Functional Relationships in Science and Technology - New Series, Volume 2 Schaifers/Voigt: Astronomy and Astrophysics / Astronomie und Astrophysik, Stars and Star Clusters / Sterne und Sternhaufen, XV. Springer-Verlag Berlin Heidelberg, New York, p. 54
Alves S. et al., 2015, MNRAS, 448, 2749
Andersen J., 1991, A&AR, 3, 91
Astropy Collaboration, 2013, A&A, 558, A33
Baines E. K., Armstrong J. T., 2012, ApJ, 744, 138
Baines E. K., McAlister H. A., ten Brummelaar T. A., Turner N. H., Sturmann J., Sturmann L., Goldfinger P. J., Ridgway S. T., 2008, ApJ, 680, 728
Behr B. B., Cenko A. T., Hajian A. R., McMillan R. S., Murison M., Meade J., Hindsley R., 2011, AJ, 142, 6
Bensby T., Feltzing S., Oey M. S., 2014, A&A, 562, A71
Bessell M. S., 2000, PASP, 112, 961
Blackwell D. E., Lynas-Gray A. E., 1998, A&AS, 129, 505
Boden A. F., Creech-Eakman M. J., Queloz D., 2000, ApJ, 536, 880
Boden A. F., Torres G., Hummel C. A., 2005, ApJ, 627, 464
Bohlin R. C., 2007, The Future of Photometric, Spectrophotometric and Polarimetric Standardization, ASP Conference Series, 364, 315, Astronomical Society of the Pacific, Sterken C,
Bonneau D. et al., 2006, A&A, 456, 789
Bonneau D., Delfosse X., Mourard D., Lafrasse S., Mella G., Cetre S., Clausse J.-M., Zins G., 2011, A&A, 535, A53
Bouquin J.-B. L. et al., 2011, A&A, 535, A67
Boyajian T. S. et al., 2012a, ApJ, 746, 101
Boyajian T. S. et al., 2012b, ApJ, 757, 112

Boyajian T. S. et al., 2013, ApJ, 771, 40
Boyajian T. S., van Belle G., von Braun K., 2014, AJ, 147, 47
Brasseur C. M., Stetson P. B., VandenBerg D. A., Casagrande L., Bono G., Dall'Ora M., 2010, AJ, 140, 1672
Gaia Collaboration et al., 2018, A&A, 616, 22
Cardelli J. A., Clayton G. C., Mathis J. S., 1989, ApJ, 345, 245
Casagrande L., VandenBerg D. A., 2014, MNRAS, 444, 392
Casagrande L., VandenBerg D. A., 2018a, MNRAS, 479, L102
Casagrande L., VandenBerg D. A., 2018b, MNRAS, 475, 5023
Casagrande L., Ramírez I., Meléndez J., Bessell M., Asplund M., 2010, A&A, 512, A54
Casagrande L., Schönrich R., Asplund M., Cassisi S., Ramírez I., Meléndez J., Bensby T., Feltzing S., 2011, A&A, 530, A138
Casagrande L., Wolf C., Mackey A. D., Nordlander T., Yong D., Bessell M., 2018, MNRAS, 482, 2770
Chen Y., Girardi L., Bressan A., Marigo P., Barbieri M., Kong X., 2014, MNRAS, 444, 2525
Claret A., 2000, A&A, 363, 1081
Claret A., Bloemen S., 2011, A&A, 529, A75
Delgado Mena E., Tsantaki M., Adibekyan V. Z., Sousa S. G., Santos N. C., González Hernández J. I., Israelian G., 2017, A&A, 606, A94
Demory B.-O. et al., 2009, A&A, 505, 205
De Silva G. M. et al., 2015, MNRAS, 449, 2604
Di Folco E., Thévenin F., Kervella P., Domiciano de Souza A., Coudé du Foresto V., Ségransan D., Morel P., 2004, A&A, 426, 601
di Folco E. et al., 2007, A&A, 475, 243
Eisenhauer F. et al., 2011, The Messenger, 143, 16
Erspamer D., North P., 2003, A&A, 398, 1121
Fressin F. et al., 2013, ApJ, 766, 81
Fritz T. K. et al., 2011, ApJ, 737, 73
Fuhrmann K., Chini R., Kaderhandt L., Chen Z., 2017, ApJ, 836, 139
Fulton B. J., Petigura E. A., 2018, AJ, 156, 264
Gaia Collaboration, 2016, A&A, 595, A2
Gallenne A. et al., 2016, A&A, 586, A35
Gallenne A. et al., 2018, A&A, 616, 68,
Gallenne A. et al., 2019, A&A, 622, A164
Gray R. O., Corbally C. J., Garrison R. F., McFadden M. T., Robinson P. E., 2003, AJ, 126, 2048
Green G. M. et al., 2015, ApJ, 810, 25
Green G. M. et al., 2018, MNRAS, 478, 651
Gustafsson B., Edvardsson B., Eriksson K., Jørgensen U. G., Nordlund Å., Plez B., 2008, A&A, 486, 951
Haguenauer P. et al., 2010, in Danchi W. C., Delplancke F., Rajagopal J. K., eds, Proc. SPIE Conf. Ser. Vol. 7734, Optical and Infrared Interferometry II. SPIE, Bellingham, p. 773404
Hanbury Brown R., Davis J., Lake R. J. W., Thompson R. J., 1974, MNRAS, 167, 475
Hartkopf W. I., Mason B. D., Worley C. E., 2001, AJ, 122, 3472
Hekker S., Meléndez J., 2007, A&A, 475, 1003
Ho A. Y. Q., Ness M., Hogg D. W., Rix H.-W., 2016, Astrophysics Source Code Library, record ascl:1602.010
Howard A. W. et al., 2012, ApJS, 201, 15
Huber D. et al., 2012, ApJ, 760, 32
Hunter J. D., 2007, Compu. Sci. Eng., 9, 90
Husser T.-O., Wende-von Berg S., Dreizler S., Homeier D., Reiners A., Barman T., Hauschildt P. H., 2013, A&A, 553, A6
Høg E. et al., 2000, A&A, 355, L27
Ireland M. J. et al., 2008, in Markus M., Danchi W. C., Delplancke F., eds, Proc. SPIE Conf. Ser. Vol. 7013, Optical and Infrared Interferometry. SPIE, Bellingham, p. 701324
Jenkins J. S. et al., 2011, A&A, 531, A8
Jones E., Oliphant T., Peterson P., 2016, SciPy: Open source scientific tools for Python. p. 2001
Karovicova I. et al., 2018, MNRAS, 475, L81
Kervella P., Bigot L., Gallenne A., Thévenin F., 2017, A&A, 597, A137
Kollmeier J. A. et al., 2017, preprint (arXiv:1711.03234)
Konacki M., Muterspaugh M. W., Kulkarni S. R., Hełminiak K. G., 2010, ApJ, 719, 1293
Lachaume R., Rabus M., Jordán A., 2014, in Rajagopal J. K., Creech-Eakman M. J., Malbet F., eds, Proc. SPIE Conf. Ser. Vol. 9146, Optical and Infrared Interferometry IV. SPIE, Bellingham, p. 914631
Lachaume R., Rabus M., Jordán A., Brahm R., Boyajian T., von Braun K., Berger J.-P., 2019, MNRAS, 484, 2656
Lallement R., Welsh B. Y., Vergely J. L., Crifo F., Sfeir D., 2003, A&A, 411, 447
Lebzelter T. et al., 2012, A&A, 547, A108
Leroy J. L., 1993, A&A, 274, 203
Liu Y. J., Zhao G., Shi J. R., Pietrzyński G., Gieren W., 2007, MNRAS, 382, 553
Magic Z., Weiss A., Asplund M., 2015, A&A, 573, A89
Mallik S. V., Parthasarathy M., Pati A. K., 2003, A&A, 409, 251
Mann A. W., Feiden G. A., Gaidos E., Boyajian T., von Braun K., 2015, ApJ, 804, 64
Martínez-Arnáiz R., Maldonado J., Montes D., Eiroa C., Montesinos B., 2010, A&A, 520, A79
Mason B. D., Wycoff G. L., Hartkopf W. I., Douglass G. G., Worley C. E., 2001, AJ, 122, 3466
Massarotti A., Latham D. W., Stefanik R. P., Fogel J., 2008, AJ, 135, 209
McKinney W., 2010, p. 51
Nissen P. E., Gustafsson B., 2018, A&AR, 26, 6
Nordgren T. E. et al., 1999, AJ, 118, 3032
Oliphant T. E., 2006, A guide to NumPy, Vol. 1. Trelgol Publishing, USA
Paladini C. et al., 2018, Nature, 553, 310
Pecaut M. J., Mamajek E. E., 2013, ApJS, 208, 9
Perez F., Granger B. E., 2007, Comput. Sci. Eng., 9, 21
Petigura E. A., Howard A. W., Marcy G. W., 2013, PNAS, 110, 19273
Piau L., Kervella P., Dib S., Hauschildt P., 2011, A&A, 526, A100
Pickles A. J., 1998, PASP, 110, 863
Pietrinferni A., Cassisi S., Salaris M., Castelli F., 2004, ApJ, 612, 168
Pijpers F. P., Teixeira T. C., Garcia P. J., Cunha M. S., Monteiro M. J. P. F. G., Christensen-Dalsgaard J., 2003, A&A, 406, L15
Pourbaix D. et al., 2004, A&A, 424, 727
Rabus M. et al., 2019, MNRAS, 484, 2674
Ramírez I., Allende Prieto C., Lambert D. L., 2013, ApJ, 764, 78
Royer F., Zorec J., Gómez A. E., 2007, A&A, 463, 671
Schröder C., Reiners A., Schmitt J. H. M. M., 2009, A&A, 493, 1099
Skrutskie M. F. et al., 2006, AJ, 131, 1163
Stassun K. G., Torres G., 2018, ApJ, 862, 61
ten Brummelaar T. A. et al., 2005, ApJ, 628, 453
Tomkin J., Fekel F. C., 2006, AJ, 131, 2652
Torres C. A. O., Quast G. R., da Silva L., de La Reza R., Melo C. H. F., Sterzik M., 2006, A&A, 460, 695
Torres G., Andersen J., Giménez A., 2010, A&AR, 18, 67
Valenti J. A., Fischer D. A., 2005, ApJS, 159, 141
van Belle G. T., von Braun K., 2009, ApJ, 694, 1085
van Belle G. T., Ciardi D. R., Boden A. F., 2007, ApJ, 657, 1058
van Belle G. T. et al., 2008, ApJS, 176, 276
VandenBerg D. A., Casagrande L., Stetson P. B., 2010, AJ, 140, 1020
von Braun K. et al., 2011, ApJ, 729, L26
von Braun K. et al., 2012, ApJ, 753, 171
White T. R. et al., 2013, MNRAS, 433, 1262
White T. R. et al., 2018, MNRAS, 477, 4403
Wittkowski M. et al., 2017, A&A, 601, A3
Wright E. L. et al., 2010, AJ, 140, 1868
Yong D., Lambert D. L., Prieto C. A., Paulson D. B., 2004, ApJ, 603, 697

APPENDIX A: CALIBRATORS

Table A1. Calibrator stars.

HD	SpT (Actual)[a]	SpT (Adopted)[b]	V_T^c (mag)	H^d (mag)	$E(B-V)$ (mag)	θ_{pred} (mas)	θ_{LD} Rel	Used	Plx (mas)	Target/s
9228	K2III	K2III	6.08	3.13	0.186	1.336 ± 0.07	VW3	Y	5.99 ± 0.06[e]	τ Cet
10148	F0V	F0V	5.61	4.83	0.029	0.461 ± 0.02	VW3	Y	13.89 ± 0.11[e]	τ Cet
18978	A3IV-V	A3IV	4.09	3.54	0.000	0.719 ± 0.04	VW3	Y	38.58 ± 0.39[e]	τ Cet
17206	F7V	F7V	4.52	3.24	0.000	0.904 ± 0.05	VW3	Y	70.74 ± 0.45[e]	τ Cet
18622	–	A3IV	–	–	–	–	–	N[f]	–	α Hyi, χ Eri, τ Cet
1581	F9.5V	F9V	4.29	2.74	0.000	1.151 ± 0.06	VW3	Y	117.17 ± 0.33[e]	α Hyi, χ Eri
15233	F2II/III	F2II	5.40	4.51	0.000	0.543 ± 0.03	VW3	Y	21.01 ± 0.10[e]	α Hyi
19319	F0III/IV	F0III	5.16	4.28	0.000	0.580 ± 0.03	VW3	N[f]	23.36 ± 0.12[e]	α Hyi
11332	K0III	K0III	6.25	3.71	0.004	0.795 ± 0.04	VW3	Y	6.88 ± 0.03[e]	α Hyi, χ Eri
10019	G8III	G8III	6.95	4.76	0.013	0.573 ± 0.03	VW3	Y	5.61 ± 0.03[e]	χ Eri
16970A	A2Vn	A2V	3.55	–	0.000	0.754 ± 0.03	BV-feh	Y	43.60 ± 0.82[e]	δ Eri, ϵ Eri, 95 Cet A
19866	K0III	K0III	7.21	4.73	0.178	0.583 ± 0.03	VW3	Y	5.88 ± 0.04[e]	95 Cet A
20699	K0III	K0III	6.83	4.75	−0.048	0.580 ± 0.03	VW3	Y	6.24 ± 0.04[e]	95 Cet A
19994	F8.5V	F8V	5.13	3.77	0.000	0.785 ± 0.04	VW3	Y	44.37 ± 0.20[e]	95 Cet A
22484	F9IV-V	F9IV	4.35	2.92	0.000	1.127 ± 0.06	VW3	Y	71.62 ± 0.54[c]	40 Eri A, 95 Cet A
21530	K2II/III	K2II	5.85	3.33	−0.177	1.101 ± 0.06	VW3	Y	10.59 ± 0.09[e]	ϵ Eri
25725	M7 + II	M7II	8.74	−0.32	–	–	VW4	N[h]	2.28 ± 0.68[c]	ϵ Eri
20010A	F6V	F6V	3.98	2.32	0.000	1.247 ± 0.06	VK	Y	71.68 ± 0.31[e]	δ Eri, ϵ Eri
24555	G6.5III	G6III	4.80	2.47	−0.007	1.414 ± 0.07	VK	Y	10.11 ± 0.24[e]	δ Eri, ϵ Eri
23304	K0III	K0III	7.33	4.88	0.102	0.546 ± 0.03	VW3	Y	5.25 ± 0.07[e]	δ Eri
26464	K1III	K1III	5.81	3.55	−0.011	1.039 ± 0.05	VW3	Y	10.01 ± 0.09[e]	δ Eri, 40 Eri A
24780	K4/5III	K4III	8.49	4.84	0.129	0.664 ± 0.03	VW3	Y	1.66 ± 0.05[e]	40 Eri A
26409	G8III	G8III	5.55	3.59	0.002	1.011 ± 0.05	VW3	Y	9.10 ± 0.11[e]	40 Eri A
27487	G8III	G8III	6.83	4.75	−0.011	0.560 ± 0.03	VW3	Y	4.96 ± 0.04[e]	40 Eri A
33111	A3IV	A3IV	2.78	2.44	0.000	1.241 ± 0.06	VW3	Y	36.50 ± 0.42[c]	40 Eri A
136498	K2III	K2III	7.89	4.67	0.222	0.629 ± 0.03	VW3	Y	2.27 ± 0.05[e]	37 Lib
139155	K2/3IV	K2IV	8.64	5.00	0.472	0.548 ± 0.03	VW3	Y	1.69 ± 0.06[e]	37 Lib
149757	O9.2IVnn	O9IV	2.55	2.67	0.335	0.940 ± 0.05	VW3	Y	5.83 ± 1.02[e]	37 Lib
132052	F2V	F2V	4.50	3.82	0.000	0.753 ± 0.04	VW3	Y	36.31 ± 0.26[e]	37 Lib
141795	kA2hA5mA7V	A5V	3.71	3.44	0.000	0.789 ± 0.04	VW3	Y	48.08 ± 0.57[e]	37 Lib
128898	A7VpSrCrEu	A7V	3.19	2.47	0.000	1.157 ± 0.06	VW3	Y	62.94 ± 0.43[e]	β TrA
140018	K1/2III	K1III	7.01	3.97	0.290	0.847 ± 0.04	VW3	Y	1.96 ± 0.03[e]	β TrA
143853	K1III	K1III	7.24	3.92	0.268	0.706 ± 0.04	VW3	Y	2.05 ± 0.04[e]	β TrA
136225	K3III	K3III	7.30	3.66	0.305	0.969 ± 0.05	VW3	Y	1.22 ± 0.04[e]	β TrA
165040	kA4hF0mF2III	F0III	4.36	3.80	0.000	0.681 ± 0.03	VW3	Y	24.78 ± 0.31[e]	β TrA, HR7221
166464	K0III	K0III	5.08	2.71	0.059	1.433 ± 0.07	VW3	Y	12.63 ± 0.24[e]	λ Sgr
167720	K2III	K2III	5.97	2.43	0.392	1.790 ± 0.09	VW3	Y	3.02 ± 0.17[e]	λ Sgr
175191	B2V	B2V	–	–	–	–	–	N[f]	–	λ Sgr
165634	G7:IIIbCN-1CH-3.5HK + 1	G7III	4.66	2.19	0.010	1.620 ± 0.08	VW3	Y	9.83 ± 0.34[e]	λ Sgr
169022	B9.5III	B9III	1.81	1.77	0.000	1.569 ± 0.11	VW4	Y	22.76 ± 0.24[c]	λ Sgr
192531	K0III	K0III	6.40	3.85	0.055	0.781 ± 0.04	VW3	Y	7.73 ± 0.03[e]	δ Pav

Table A1 – *continued*

HD	SpT (Actual)[a]	SpT (Adopted)[b]	V_T^c (mag)	H^d (mag)	$E(B-V)$ (mag)	θ_{pred} (mas)	θ_{LD} Rel	Used	Plx (mas)	Target/s
197051	A7III	A7III	3.43	2.79	0.000	0.982 ± 0.05	VW3	Y	25.64 ± 0.33[e]	δ Pav, ϵ Ind
197359	K0/1III	K0III	6.82	4.47	0.074	0.674 ± 0.03	VW3	Y	6.26 ± 0.03[e]	δ Pav
169326	K2III	K2III	6.09	3.50	0.028	1.089 ± 0.06	VW3	Y	6.66 ± 0.08[e]	δ Pav
191937	K3III	K3III	6.72	3.57	0.157	1.084 ± 0.06	VW3	Y	3.99 ± 0.03[e]	δ Pav
205935	K0II/III	K0II	6.45	3.95	−0.016	0.829 ± 0.04	VW3	Y	4.96 ± 0.03[e]	ϵ Ind
209952	B6V	B6V	1.76	2.03	0.000	1.112 ± 0.08	VW4	Y	32.29 ± 0.21[c]	ϵ Ind
212878	G8III	G8III	6.98	4.81	0.035	0.553 ± 0.03	VW3	Y	5.11 ± 0.04[e]	ϵ Ind
219571	F4V	F4V	4.03	3.08	0.000	1.077 ± 0.05	VW3	Y	42.32 ± 0.25[e]	ϵ Ind
4188	K0III	K0III	4.88	2.67	0.000	1.476 ± 0.08	VW3	Y	14.41 ± 0.37[e]	τ Cet
129008	G8III/IV	G8III	7.25	4.88	0.029	0.546 ± 0.03	VW3	Y	5.88 ± 0.05[e]	HD131977
133649	K0III	K0III	7.81	4.96	0.188	0.528 ± 0.03	VW3	Y	2.81 ± 0.05[e]	HD131977
133670	K0III	K0III	6.25	3.83	0.000	0.851 ± 0.04	VW3	Y	15.41 ± 0.06[e]	HD131977
129502	F2V	F2V	3.91	3.07	0.000	1.087 ± 0.06	VW3	Y	54.79 ± 0.51[e]	HD131977
133627	K0III	K0III	6.86	4.33	0.041	0.709 ± 0.04	VW3	Y	6.58 ± 0.05[e]	HD131977
152236	B1Ia-0ek	B1Ia	4.82	3.34	0.615	–	–	N[g]	0.71 ± 0.24[e]	η Sco
152293	F3II	F3II	5.91	4.25	0.294	0.604 ± 0.03	VW3	Y	0.31 ± 0.16[e]	η Sco
158408	B2IV	B2IV	2.62	3.11	0.051	–	–	N[f]	5.66 ± 0.18[c]	η Sco
135382	A1V	A1V	2.85	2.53	0.000	1.090 ± 0.06	VW3	Y	16.50 ± 0.73[e]	η Sco
160032	F4V	F4V	4.80	3.70	0.000	0.743 ± 0.04	VW3	Y	47.10 ± 0.29[e]	η Sco
182835	F2Ib	F2Ib	4.73	2.87	0.339	1.063 ± 0.05	VW3	Y	1.29 ± 0.22[e]	β Aql
193329	K0III	K0III	6.16	3.83	0.091	0.910 ± 0.05	VW3	Y	7.90 ± 0.07[e]	β Aql
189533	G8II	G8II	6.84	3.74	0.295	0.864 ± 0.04	VW3	Y	2.42 ± 0.04[e]	β Aql
189188	K2III	K2III	6.89	3.73	0.071	0.857 ± 0.04	VW3	Y	4.49 ± 0.04[e]	β Aql
194013	G8III-IV	G8III	5.41	3.31	0.038	1.143 ± 0.06	VW3	Y	12.59 ± 0.14[e]	β Aql
172555	A7V	A7V	4.79	4.25	0.000	0.792 ± 0.04	VW3	N[g]	35.29 ± 0.23[e]	HR7221
173948	B2Ve	B2V	4.18	4.32	0.051	0.419 ± 0.02	VW3	Y	4.80 ± 0.45[e]	HR7221
161955	K0/1III	K0III	6.58	4.10	0.100	0.746 ± 0.04	VW3	Y	6.85 ± 0.04[e]	HR7221
188228	A0Va	A0V	3.94	3.76	0.000	0.571 ± 0.03	VW3	Y	31.87 ± 0.33[e]	HR7221

Notes. [a]SIMBAD.
[b]Adopted for intrinsic colour grid interpolation.
[c]Tycho Høg et al. (2000).
[d]2MASS Skrutskie et al. (2006).
[e]Gaia Brown et al. (2018).
[f]Binarity.
[g]IR excess.
[h]Inconsistent photometry.

APPENDIX B: BOLOMETRIC FLUXES

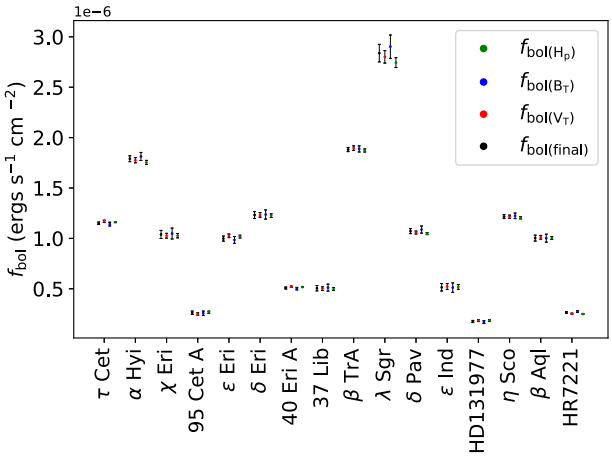

Figure B1. Comparison of f_{bol} calculated from *Hipparcos*–Tycho H_P, B_T, V_T, as compared to the final average value adopted.

Table B1. Calculated bolometric fluxes.

Star	HD	f_{bol} (MARCS) (10^{-8} erg s^{-1} cm^{-2})	$\sigma_{f_{bol}}(\zeta)$ (per cent)
τ Cet	10700	<>: 114.976	1.08
		H_p: 116.099	0.40
		B_T: 114.227	1.64
		V_T: 116.981	0.94
α Hyi	12311	<>: 178.994	1.66
		H_p: 175.530	1.12
		B_T: 181.304	2.23
		V_T: 177.571	1.43
χ Eri	11937	<>: 103.957	3.85
		H_p: 102.641	2.02
		B_T: 104.834	5.15
		V_T: 102.741	2.33
95 Cet A	20559	<>: 26.195	6.37
		H_p: 26.783	3.91
		B_T: 25.803	8.16
		V_T: 25.088	4.65
ϵ Eri	22049	<>: 99.817	2.52
		H_p: 101.793	1.36
		B_T: 98.500	3.40
		V_T: 102.539	1.76
δ Eri	23249	<>: 123.239	2.75
		H_p: 122.583	1.45
		B_T: 123.676	3.66
		V_T: 123.326	1.82
40 Eri A	26965	<>: 50.797	1.84
		H_p: 51.708	0.92
		B_T: 50.189	2.56
		V_T: 52.095	1.31
37 Lib	138716	<>: 50.601	5.23
		H_p: 49.763	3.00
		B_T: 51.159	6.76
		V_T: 50.133	3.54
β TrA	141891	<>: 188.174	1.14
		H_p: 187.285	0.82
		B_T: 188.766	1.60
		V_T: 189.549	1.20
λ Sgr	169916	<>: 283.889	3.08
		H_p: 274.369	1.77
		B_T: 290.236	3.99
		V_T: 280.120	2.19
δ Pav	190248	<>: 107.160	2.33
		H_p: 104.741	1.03
		B_T: 108.773	3.23
		V_T: 105.819	1.37
ϵ Ind	209100	<>: 51.481	7.18
		H_p: 51.882	4.50
		B_T: 51.214	9.04
		V_T: 52.269	5.45
HD131977	131977	<>: 17.554	6.40
		H_p: 18.572	4.77
		B_T: 16.876	8.07
		V_T: 18.358	4.82
η Sco	155203	<>: 121.621	1.62
		H_p: 120.550	0.97
		B_T: 122.336	2.28
		V_T: 121.489	1.32
β Aql	188512	<>: 100.299	2.90
		H_p: 100.388	1.49
		B_T: 100.239	3.93
		V_T: 101.120	1.81
HR7221	177389	<>: 26.462	2.81
		H_p: 24.930	1.53
		B_T: 27.484	3.65
		V_T: 25.323	1.92

APPENDIX C: LIMB DARKENING

Table C1. Comparison between θ_{LD} derived using Claret & Bloemen (2011) linear limb darkening coefficients and Magic et al. (2015) equivalent linear limb darkening coefficients. The absolute median percentage difference is 0.14 per cent, with no obvious systematic observed. The largest discrepancy is for λ Sgr, our most well-resolved star.

Star	$\theta_{LD,CB11}$ (mas)	$\theta_{LD,STAGGER}$ (mas)	$\sigma_{\theta_{LD}}$ (%)
τ Cet	2.053 ± 0.011	2.054 ± 0.011	−0.07
χ Eri	2.139 ± 0.012	2.134 ± 0.011	0.25
95 Cet A	1.277 ± 0.012	1.280 ± 0.012	−0.26
ϵ Eri	2.146 ± 0.012	2.144 ± 0.011	0.08
δ Eri	2.413 ± 0.010	2.411 ± 0.009	0.08
40 Eri A	1.489 ± 0.012	1.486 ± 0.012	0.23
37 Lib	1.687 ± 0.010	1.684 ± 0.010	0.14
λ Sgr	4.074 ± 0.019	4.060 ± 0.015	0.35
δ Pav	1.826 ± 0.025	1.828 ± 0.025	−0.07
β Aql	2.137 ± 0.012	2.133 ± 0.012	0.18
HR7221	1.116 ± 0.015	1.117 ± 0.015	−0.14

Table C2. Limb darkening coefficients.

Star	CB11	Equivalent linear limb darkening coefficient						θ_{LD} scaling term					
	u_λ	u_{λ_1}	u_{λ_2}	u_{λ_3}	u_{λ_4}	u_{λ_5}	u_{λ_6}	s_{λ_1}	s_{λ_2}	s_{λ_3}	s_{λ_4}	s_{λ_5}	s_{λ_6}
τ Cet	–	0.247 ± 0.001	0.234 ± 0.001	0.221 ± 0.001	0.215 ± 0.001	0.210 ± 0.001	0.212 ± 0.001	0.994	0.995	0.995	0.995	0.995	0.995
α Hyi	0.211 ± 0.015	–	–	–	–	–	–	–	–	–	–	–	–
χ Eri	–	0.267 ± 0.006	0.251 ± 0.005	0.233 ± 0.005	0.227 ± 0.004	0.221 ± 0.004	0.226 ± 0.004	0.994	0.994	0.994	0.994	0.995	0.995
95 Cet A	–	0.313 ± 0.007	0.292 ± 0.006	0.268 ± 0.006	0.260 ± 0.006	0.253 ± 0.005	0.253 ± 0.005	0.993	0.993	0.993	0.994	0.994	0.994
ϵ Eri	–	0.275 ± 0.003	0.258 ± 0.002	0.243 ± 0.002	0.237 ± 0.002	0.231 ± 0.002	0.232 ± 0.002	0.994	0.994	0.994	0.994	0.994	0.994
δ Eri	–	0.282 ± 0.004	0.264 ± 0.004	0.245 ± 0.004	0.239 ± 0.003	0.232 ± 0.003	0.237 ± 0.003	0.994	0.994	0.994	0.994	0.994	0.994
40 Eri A	–	0.263 ± 0.002	0.248 ± 0.002	0.234 ± 0.002	0.227 ± 0.002	0.222 ± 0.002	0.224 ± 0.001	0.994	0.994	0.994	0.994	0.995	0.995
37 Lib	–	0.298 ± 0.007	0.279 ± 0.006	0.257 ± 0.006	0.250 ± 0.005	0.243 ± 0.005	0.245 ± 0.005	0.993	0.994	0.994	0.994	0.994	0.994
β TrA	0.209 ± 0.011	–	–	–	–	–	–	–	–	–	–	–	–
λ Sgr	–	0.307 ± 0.004	0.287 ± 0.003	0.263 ± 0.003	0.256 ± 0.003	0.248 ± 0.003	0.249 ± 0.003	0.993	0.993	0.994	0.994	0.994	0.994
δ Pav	–	0.251 ± 0.004	0.239 ± 0.004	0.226 ± 0.004	0.219 ± 0.004	0.213 ± 0.004	0.218 ± 0.003	0.994	0.995	0.995	0.995	0.995	0.995
ϵ Ind	0.382 ± 0.021	–	–	–	–	–	–	–	–	–	–	–	–
HD131977	0.359 ± 0.031	–	–	–	–	–	–	–	–	–	–	–	–
η Sco	0.215 ± 0.017	–	–	–	–	–	–	–	–	–	–	–	–
β Aql	–	0.266 ± 0.005	0.250 ± 0.004	0.233 ± 0.004	0.227 ± 0.004	0.221 ± 0.004	0.225 ± 0.003	0.994	0.994	0.994	0.995	0.995	0.995
HR7221	–	0.290 ± 0.004	0.271 ± 0.003	0.251 ± 0.003	0.245 ± 0.003	0.238 ± 0.003	0.241 ± 0.003	0.993	0.994	0.994	0.994	0.994	0.994

This paper has been typeset from a TEX/LATEX file prepared by the author.